

PHYSICAL VOLCANOLOGY OF THE 1666 C.E. CINDER CONE ERUPTION,
LASSEN VOLCANIC NATIONAL PARK, CA

by

JESSICA KATHARINE MARKS

A THESIS

Presented to the Department of Geological Sciences
and the Graduate School of the University of Oregon
in partial fulfillment of the requirements
for the degree of
Master of Science

September 2012

THESIS APPROVAL PAGE

Student: Jessica Katharine Marks

Title: Physical Volcanology of the 1666 C.E. Cinder Cone Eruption, Lassen Volcanic National Park, CA

This thesis has been accepted and approved in partial fulfillment of the requirements for the Master of Science degree in the Department of Geological Sciences by:

Dr. Katharine Cashman	Chair
Dr. Paul Wallace	Member
Dr. Mark Reed	Member

and

Kimberly Andrews Espy	Vice President for Research & Innovation/Dean of the Graduate School
-----------------------	--

Original approval signatures are on file with the University of Oregon Graduate School.

Degree awarded September 2012

© 2012 Jessica Katharine Marks

THESIS ABSTRACT

Jessica Katharine Marks

Master of Science

Department of Geological Sciences

September 2012

Title: Physical Volcanology of the 1666 C.E. Cinder Cone Eruption, Lassen Volcanic National Park, CA

Cinder Cone is the most recent cinder cone eruption in the continental United States at ~350 years old. This study examines the physical characteristics of the explosive deposit of the volcano in order to infer eruption timing, style, and mechanisms. Building on previous work and using spatial extent, field relationships, and grain size, componentry, and textural data of ten samples from one column, this study demonstrates that Cinder Cone erupted in at least two distinct phases with at least two distinct eruption styles. This speaks to the changing magma supply and transport processes occurring beneath the volcano. Curiosities about the eruption include the extensive degree of contamination that contributed abundant quartz xenocrysts to all the deposits. Future work includes determining the extent and mechanism/s of contamination and tephra component creation. These data are important for informing hazard assessments of areas with abundant cinder cone volcanoes.

CURRICULUM VITAE

NAME OF AUTHOR: Jessica Katharine Marks

GRADUATE AND UNDERGRADUATE SCHOOLS ATTENDED

University of Oregon, Eugene, OR
Carleton College, Northfield, MN

DEGREES AWARDED:

Master of Science, Geology, 2012, University of Oregon
Bachelor of Arts, Geology, 2009, Carleton College

AREAS OF SPECIAL INTEREST:

Volcanology
Physical volcanology

PROFESSIONAL EXPERIENCE:

Kilauea Geology Group volunteer, Hawaiian Volcano Observatory, 2009

Intern, Department of Earth and Planetary Sciences, American Museum of Natural History, New York, NY, 2008

Teaching assistant, Geology Department, Carleton College, 2007-2008

GRANTS, AWARDS, AND HONORS:

Johnston Scholarship, University of Oregon, Department of Geological Sciences, 2012

Graduate Teaching Fellowship, Geological Sciences, 2010 to present

Magna cum Laude, Carleton College, 2009

Phi Beta Kappa, Carleton College, 2009

Duncan Stewart Fellowship in Geology, Carleton College, 2008

Mike Ewers Award, Minnesota Space Grant Consortium, 2008

Robert J. Kolenkow and Robert A. Reitz Fund for Undergraduate Research,
Carleton College, 2009

ACKNOWLEDGMENTS

I would like to give many, many thanks to my advisor, Kathy Cashman, for all of the time she has spent helping me through this process. She has been so helpful and encouraging and full of wonderful advice. My committee members, Paul Wallace and Mark Reed, also deserve many thanks for their time, comments, and insightful questions that helped to drive my thinking. The office staff at University of Oregon – Shari, Dave, and Vicki – have been instrumental in figuring out the details of graduate school life and providing daily laughter and conversation. UO DoGS graduate students and professors have been wonderful and create a welcoming and friendly atmosphere in which to work; I am so thankful to have such an awesome department. My non-UO family and friends must also be thanked for their constant support and encouragement from near and far. This work was funded by the UO Department of Geology and NSF grant 1019848, and for that, I am eternally grateful.

TABLE OF CONTENTS

Chapter	Page
I. INTRODUCTION	1
1.1. Eruption Style	1
1.2. Characteristics of Cinder Cone Fields	4
1.3. Cinder Cone, LAVO	6
II. METHODS	13
2.1. Field Methods	13
2.2. Laboratory Methods.....	15
III. RESULTS	20
3.1. Field Results	20
3.2. Laboratory Results.....	23
IV. DISCUSSION.....	35
4.1. Deposit Characteristics	35
4.1.1. Spatial Distribution of Eruptive Units	36
4.1.2. Sequence of Events.....	40
4.1.3. Grain Size Characteristics.....	44
4.1.4. Deposit Components.....	44
4.2. Textural Analysis.....	48
4.3. Eruption Chronology	54
4.4. Eruptive Styles.....	61

Chapter	Page
4.4.1. Formation of Different Components.....	62
V. CONCLUSIONS	68
REFERENCES CITED.....	70

LIST OF FIGURES

Figure	Page
1. Comparison of isopach data from cinder cones	3
2. Map of Cinder Cone.....	7
3. M. Clynne’s (USGS) bulk compositional data	11
4. Field photo of the main column, LCC-1	14
5. Map highlighting the spatial difference between tephra Units 2 and 3	16
6. Photos of three main tephra components	17
7. Comparison between the original image and the cleaned and traced image	19
8. Simplified stratigraphic column shown with data from this study	21
9. Proximal and distal field photos of pits dug	24
10. Field photos.....	25
11. SEM image of sample LCC-1-1G.....	27
12. SEM image of a quartz crystal with a pyroxene reaction rim.....	28
13. Comparative SEM images of the three components.....	29
14. Stratigraphic comparison of SEM images	31
15. Histograms in percent	34
16. A thickness versus square root of area isopach plot	37
17. Schematic stratigraphic columns	41
18. A median diameter versus sorting (both in Φ units) plot.....	45
19. Componentry data of Cinder Cone and other mafic cinder cone volcanoes.....	47
20. Schematic plot of crystallinity versus crystal number density.....	49
21. Crystallinity plotted against crystal number density for mafic crystals.....	50
22. Phase diagram	51
23. Crystallinity and CND plotted against $Md\Phi$ and % golden tephra	53
24. Revised trends in the bulk geochemistry of lava and tephra	57
25. Plot showing bulk composition data as well as melt inclusion data	58
26. Volatile data	60
27. SEM images	66

LIST OF TABLES

Table	Page
1. Descriptions used to perform componentry on grainsize fractions >1mm	15
2. Field descriptions of layers where samples were taken	20
3. Composition used to create phase diagram (Fig. 22).....	52

CHAPTER I

INTRODUCTION

By number, cinder cones are one of the most prevalent volcanic landforms on the planet. Within certain tectonic environments, they may form anywhere at anytime (e.g. Parícutin in Mexico, see Foshag and González, 1956 and Luhr and Simkin, 1993) thereby posing significant hazards in locations prone to cinder cone development. Cinder cones are commonly assumed to exhibit Strombolian eruption styles (Lockwood and Hazlett, 2010), although a much wider variety of eruptive style has been observed (e.g. Hill et al., 1998; Pioli et al., 2008). Improving our understanding of the range of eruptive activity that cinder cones may produce will aid hazard assessment of cinder cone fields. Toward this end, I have studied the eruption of a specific cinder cone, one called Cinder Cone in Lassen Volcanic National Park (LAVO), CA, USA. My goal is to use the eruptive deposits to constrain both the timing and nature of different explosive styles of activity that occurred as Cinder Cone formed. I focus primarily on the tephra deposit, as tephra can have the most far-reaching impacts on surrounding areas (e.g. Houghton et al., 2006).

1.1. Eruption Style

Strombolian eruptions are moderately explosive and produce ash, scoria, and bombs that are still incandescent as they leave the vent. These eruptions are episodic and generally caused by large gas bubbles bursting that create steam-rich ash clouds (Lockwood and Hazlett, 2010); they generate tephra with mean sizes ranging from 150 μm to 10 cm (McGetchin et al., 1974). In contrast, less explosive Hawaiian eruptions are

primarily effusive with lava fountaining events that generate larger, more vesicular clasts, whereas more explosive violent Strombolian eruptions produce greater quantities of ash (Lockwood and Hazlett, 2010). The type example of a violent Strombolian eruption is the 1943-1952 eruption of Parícutin volcano, Mexico (Macdonald, 1972; Walker, 1973). Violent Strombolian activity is strongly pulsatory with simultaneous tephra and lava extrusion and the production of ash-rich plumes between 2 and 6 kilometers in height (e.g., Pioli et al., 2008). This simultaneous tephra and lava emission is probably caused by shallow gas segregation beneath the volcanic edifice (Krauskopf, 1948; Pioli et al., 2009).

Explosive eruption styles may be distinguished by measuring the physical characteristics of tephra deposits. For example, a plot of log tephra thickness (isopach thickness) vs. $\sqrt{\text{area}}$ commonly yields linear trends with slopes that reflect the areal coverage, a measure of eruption intensity (Fig. 1). The exponential form of tephra deposit thinning allows estimation of tephra volumes by integrating under the curve. Figure 1 shows isopach data collected from cinder cones that displayed different eruption styles. Basaltic subplinian and Plinian eruptions are also shown for comparison. As shown, cinder cones exhibit a variety of eruptions styles – from cone-building Hawaiian and Strombolian to blanket-forming violent Strombolian. These more explosive violent Strombolian deposits are strikingly similar to eruptions denoted subplinian and Plinian, though violent Strombolian deposits represent tephra accumulated over weeks to months to years of activity, instead of deposition in a single eruptive event (hours to days).

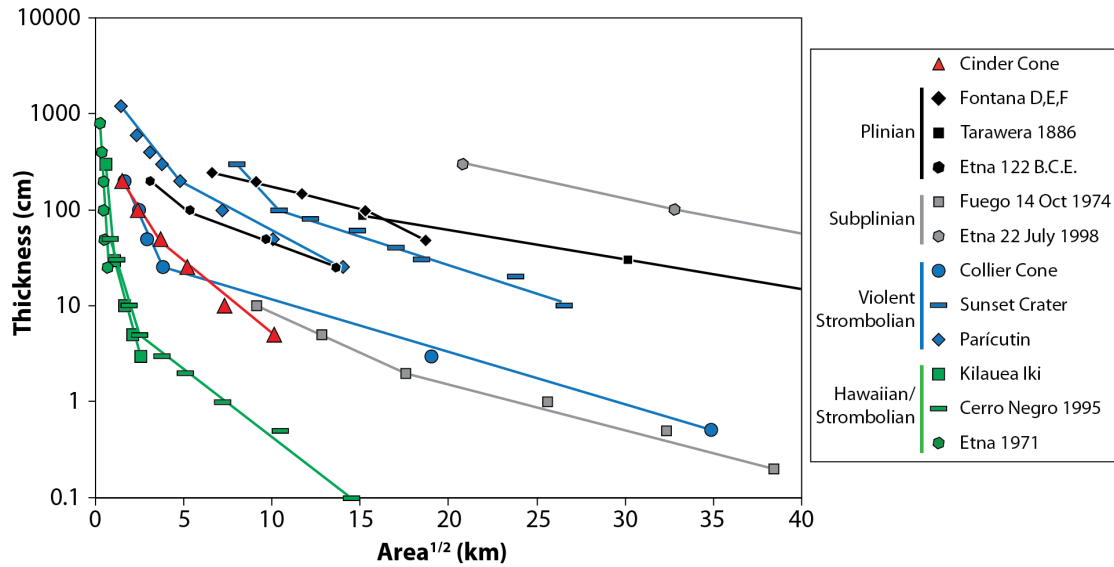


Figure 1. Comparison of isopach data from cinder cones (colors) as well as other basaltic explosive eruptions (greyscale) based on the method of Pyle (1989). This plot highlights differences in volcanic deposits that speak to differing eruption styles, as well as the range in cinder cone eruptive capability. Cinder Cone, LAVA is highlighted (red) and compared with Hawaiian/Strombolian (green) and violent Strombolian (blue) eruptions/deposits, which are then compared with basaltic subplinian (grey) and Plinian (black) deposits. Notice that the distal portion of Cinder Cone’s deposit behaves more similarly to violent Strombolian and subplinian deposits than to Hawaiian/Strombolian deposits, and that subplinian, violent Strombolian, and Plinian eruptions all vary widely in thickness and spatial area. References: Cinder Cone, *Heiken (1978)*; Fontana, *Costantini et al. (2009)*; Tarawera 1886 and Etna 122 B.C.E., *Houghton et al. (2004)*; Fuego 14 October 1974, *Rose et al. (2008)*; Etna 22 July 1998, *Andronico and Cristaldi (2009)*; Collier Cone, *D. McKay, pers. comm.*; Sunset Crater, *Ort et al. (2008)*; Parícutin, *Pioli et al. (2008)*; Kilauea Iki, *Parfitt (1998)*; Cerro Negro 1995, *Hill et al. (1998)*; Etna 1971, *Booth and Walker (1973)*.

1.2. Characteristics of Cinder Cone Fields

Previous studies of cinder cones and cinder cone fields have focused on a variety of morphological, causal, eruptive, and hazard-related aspects of cinder cone creation and erosion. Valentine et al. (2005) studied cone deposits of Lathrop Wells Volcano in Nevada, USA and found that the bulk of the cone is composed of fine-grained, unwelded layers. They inferred that the eruptions that deposited those layers must have been sustained eruption columns that would have deposited tephra tens of kilometers away, contrary to the more mild Strombolian eruptions usually thought to erupt from cinder cones. Geochemical data from tephra of the eruption of the Udo tuff cone off of Jeju Island of South Korea show that the earliest magma to erupt was more evolved in composition and the eruption progressed to more primitive compositions then back to evolved by the end (Brenna et al., 2010). It is hypothesized that these changes resulted from a single magma batch rising through a central conduit, but that the eruption tapped the magma batch's head, then core, then margins. After the explosive eruption, Udo tuff cone produced subalkaline lava flows, in contrast to the alkaline tephra. The workers infer that the volcano tapped different sources within the upper mantle, that those magmas evolved differently, and that the movement and eruption of the alkaline magma opened the conduit for the subalkaline magma (Brenna et al., 2010). Kervyn et al. (2012) morphometrically characterize cinder cone fields and find that cinder cone shapes and sizes vary widely, and should not be used to infer age without other supporting evidence. This range in cinder cone morphology reinforces the variety of eruptive behavior found at cinder cones.

The eruption of Parícutin in Mexico in 1943 is the most famous cinder cone eruption of modern history. Parícutin is situated in the western Michoacán-Guanajuato Volcanic Field (MGVF), which is a 40,000 km² part of the Mexican Volcanic Belt (MVB) with a high concentration of cinder cones (~900 of ~1,000 vents) and low concentration of large composite volcanoes normally prevalent in the MVB (Hasenaka and Carmichael, 1985). Pioli et al. (2008) completed a detailed study on a Parícutin, including the physical characteristics of the tephra, in order to characterize its eruption as the type example of the violent Strombolian style. This study tied eyewitness observations and data collected during the eruption to the deposits left behind 50 years later. This is important because it provides a vital link between deposit and eruption characteristics (as explained above). Parícutin's tephra deposit comprises finely stratified millimeter- to decimeter-sized ash and lapilli layers. Individual layers may be traced radially away from the vent, but have narrow lateral extents. Pioli et al. (2008) identified three main components: tan clasts (lowest density, irregularly shaped, few microphenocrysts), black clasts (medium density, subrounded shapes, fewer bubbles, increased crystallinity), and dense clasts (angular, highly crystalline). Lapilli layers produced during early and middle activity have median grain sizes (Md Φ) of 0-1 (1-2mm) while ash layers have Md Φ of 2-1 (0.25-0.5mm); tan clasts are the most abundant during these phases. The later phase produced coarse ash layers of Md Φ = 0 (1mm) and fine ash layers of Md Φ > 3 (<0.125mm) and is dominated by black and dense clasts. Thus, the relative abundance of ash layers increased as the eruption progressed, though Parícutin produced abundant fine ash throughout its eruption, earning the categorization of violent Strombolian (as mentioned above).

1.3. Cinder Cone, LAVO

Lassen Volcanic National Park encompasses 430 km² of volcanically-shaped landscape surrounded by the Sacramento Valley and Klamath Mountains to the west, the Sierra Nevada to the south, and the Basin and Range to the east. Lassen comprises the southernmost active volcanism of the Cascade Arc. Volcanism is generated by both the subduction of the Juan de Fuca plate beneath the North American plate, which produces the more voluminous calc-alkaline lavas, and Basin and Range extension, which produces tholeiitic lavas. Strike-slip faulting related to the San Andreas and movement between the North American and Pacific plates may also influence the tectonics and volcanism of the area (Clynne and Muffler, 2010). Overlapping lavas from the Lassen region have created a broad platform of mafic to intermediate volcanoes and volcanic products 2-4 km thick (Berge and Stauber, 1987). Constant modeled seismic velocities across the Sierra Nevada-Cascade Range boundary suggest that the Sierran basement continues underneath the southern Cascades (Berge and Stauber, 1987).

Cinder Cone is a basaltic andesite scoria cone situated in the northeast corner of LAVO, 17 kilometers from Lassen Peak (Fig. 2). It is the youngest cinder cone in the Cascade Arc, as well as in the continental United States, and thus provides a unique natural laboratory. The eruptive material comprises a ~200-meter-tall scoria cone built on top of an earlier cone, a tephra deposit up to ~3 meters deep and ~20 by ~10 kilometers in spatial extent, and five main lava flows separated into three phases – Old Bench, Painted Dunes, and Fantastic Lava (OB, PD, and FL, respectively; Clynne and Muffler, 2010). The buried cone was probably associated with the Old Bench flow, and is now

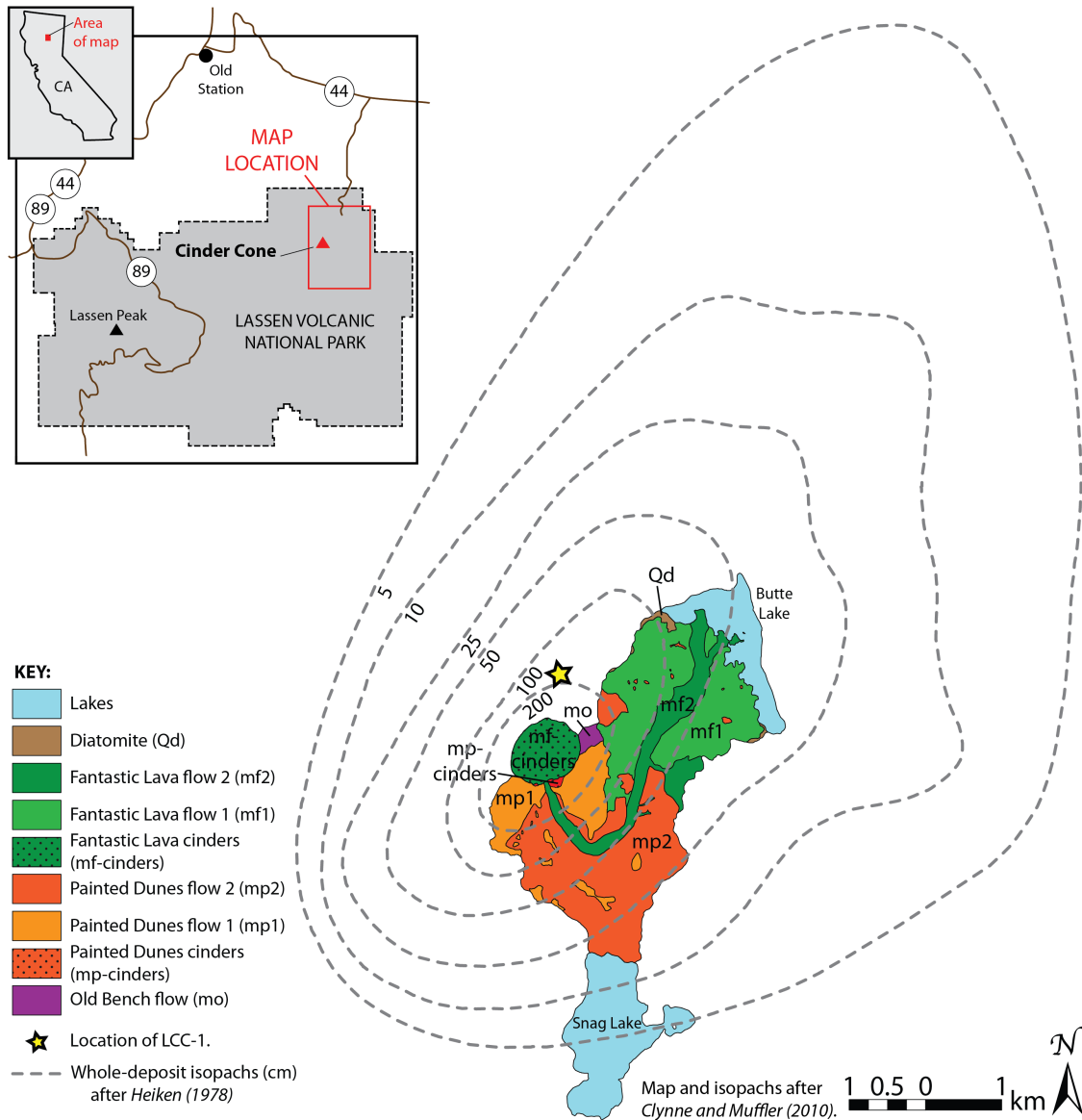


Figure 2. Map of Cinder Cone, the distribution and geology of the lava flows, and the whole-deposit tephra isopachs. The main column of this study, LCC-1, is shown as the yellow star. The three phases of the lava flows are colored here; these colors will be used to denote tephra Units and will be utilized throughout the rest of the study. Purple = Old Bench (tephra Unit 1), orange = Painted Dunes (tephra Unit 2), and green = Fantastic Lava (tephra Unit 3).

completely covered by the deposits from subsequent eruptions. The Painted Dunes and Fantastic Lava flows, and most of the tephra, were emitted from the current cone.

Diller (1891) was the first scientist to study Cinder Cone. He noted an unusual characteristic of the basalt lava, which is that it contains phenocrystic quartz crystals, although he (mistakenly) thought that the crystals had formed from the basalt. He concluded that the eruption occurred in two temporally and stylistically distinct phases. Importantly, he separated an early explosive phase that deposited the tephra, which “probably occurred nearly a hundred years before the American Revolution,” from an effusive phase that “took place at a much later date, but certainly more than 50 years ago.” His evidence for a time break was the presence of lake deposits on top of the tephra. However, this observation was later shown to be incorrect.

Finch and Anderson (1930) also commented on the curious quartz-filled lavas, hypothesizing that the basalts were “hybrid” lavas that formed from the mixing of a differentiated dacitic magma (evidenced by xenoliths and the quartz xenocrysts) with “basalt of low silica content” (based on chemical composition and dominance of olivine and pyroxene phenocrysts). They concurred with Diller (1891)’s interpretation that the eruption occurred in two stages, but suggested that the most recent lavas were erupted in the winter of 1850-1851. However, Diller (1891) stated that the eyewitness accounts of this event had a “very unsatisfactory character.”

As intimated above, a major controversy surrounding Cinder Cone has been the age and timeline of Cinder Cone’s creation. Finch (1937) found dead trees rooted in the soil beneath the tephra blanket as well as trees rooted in the tephra to assign date ranges to the eruption – a yellow pine survived 20-30 inches of tephra fall to die in 1932 and its

earliest ring dates back to 1485 C.E., while the oldest trees rooted in Cinder Cone tephra are at least 250 years old. The yellow pine also showed diminutions in growth around the years 1567 and 1666. Additionally, Finch (1937) found trees presumably killed by lava flows and calculated their ages and death dates, and ultimately hypothesized that the explosive and the effusive phases occurred in five separate stages, the earliest being an explosion in 1567 C.E. and the latest being the previously described 1851 C.E. lava flow. Clynne et al. (2000) reinterpreted the Cinder Cone deposits as having been erupted in one event. They used new radiocarbon dates of trees killed by Cinder Cone tephra and lava flows (especially an aspen mostly covered by Fantastic Lava that directly dates the eruption) to suggest that the date of 1666 C.E. inferred by Diller (1891) and Finch (1937) for the “second explosive eruption” was close to the correct date for the whole eruption (see also Clynne et al., 2002). Sheppard et al. (2009) verified this date by using additional dendrochronological analyses – ring width and ring chemistry – of old trees still growing in Cinder Cone tephra as well as control trees outside of the Cinder Cone deposits. By controlling for macroclimate of the area and incorporating changes in chemistry, Sheppard et al. (2009) narrowed down the possible causes of the changes seen and confidently confirms that 1666 C.E. is a valid date for the eruption of Cinder Cone.

Diller (1891) first described major color and morphological differences between the “lower” and “upper” parts of the tephra deposit. Heiken (1978) extended this description by completing a detailed analysis of the physical characteristics and extent of the tephra deposit. He separated the deposit into three phases (Units 1-3) that are thought to correspond with the three phases of lava flow emplacement. He notes that Unit 1 is the least widespread and was therefore probably eroded away during an eruptive pause, and

that Unit 3 is the most voluminous and widespread of the three tephra units. He also recognized three tephra components: light brown sideromelane (up to 70% vesicles with few crystals), medium brown sideromelane (30-40% vesicles with greater degrees of crystallization), and tachylite (15-20% vesicles and completely crystalline). Heiken (1978) describes Unit 1 as black to brown medium to coarse vitric ash, Unit 2 as highly vesicular light brown sideromelane bombs and lapilli interbedded with dark grey coarse ash, and Unit 3 as interbedded and graded, grey and brown coarse ash layers. He describes the eruption as predominantly Strombolian in nature, with a few Hawaiian episodes.

Heiken (1978) also identified a time gap between Unit 1 and Unit 2, when much of Unit 1 tephra was eroded away. He associated Units 2 and 3 with the Old Bench and Painted Dunes flows, respectively, because he noticed that there appeared to be little tephra associated with the Fantastic Lava flows. However, Clynne and Bleick (2011)'s geochemical data (Fig. 3) suggest instead that tephra Unit 1 should be associated with the Old Bench flow, Unit 2 with the Painted Dunes flows, and Unit 3 with the Fantastic Lava flows. Resolving this discrepancy between field-based and geochemical-based interpretations of the temporal evolution of the eruption is a primary goal of this research.

As mentioned, there are several curiosities about Cinder Cone's deposits and therefore its eruption. First, there are ubiquitous quartz xenocrysts in all of the basalt-basaltic andesite lava flows and tephra layers (Clynne et al., 2000). Second, the bulk composition of erupted material changed from basalt to basaltic andesite through the PD flows and from basaltic andesite to basalt through the FL flows (Fig. 3; Clynne et al.,

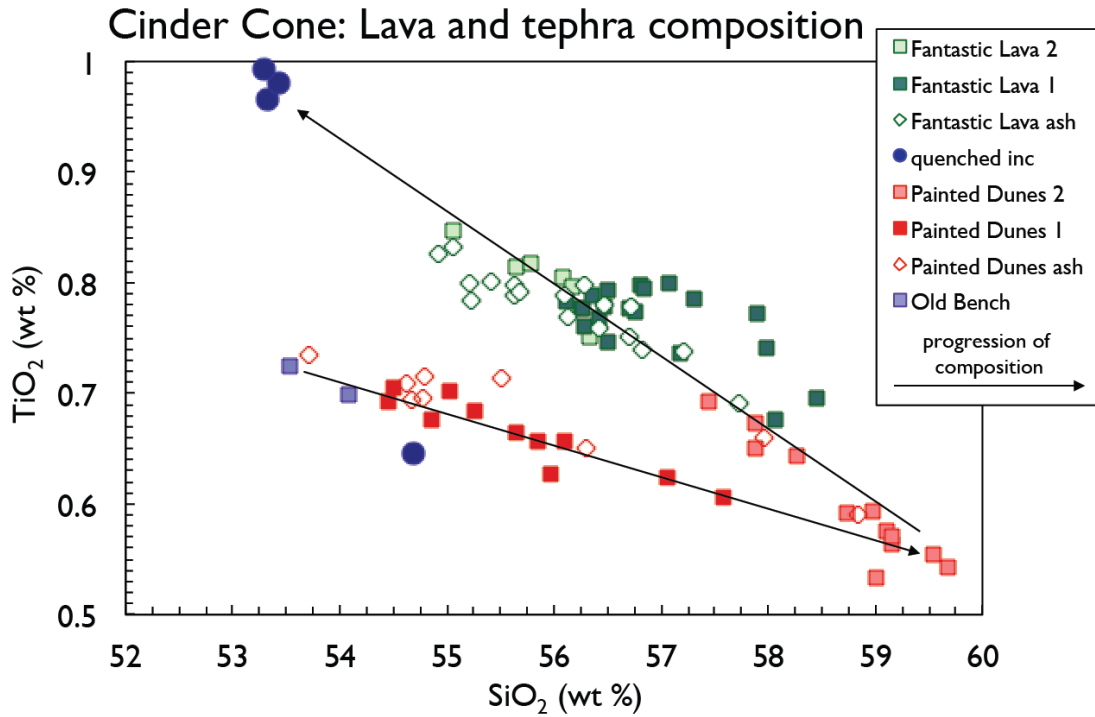


Figure 3. M. Clynne's (USGS) bulk compositional data showing the geochemical pattern throughout the eruption as well as the correlation between the lava and the tephra. This is important information in determining the timing of the eruption (M. Clynne, pers. comm.; Clynne and Bleick, 2011).

2011). The tephra mimic these changes: tephra Unit 2 is compositionally similar to the PD flows and tephra Unit 3 is compositionally similar to the FL flows (Fig. 3). However, there exist meters of tephra on the PD1 flow - the basal layers are in fact welded to the lava - and very little on the rest of the flows (PD2, FL1 and FL2). The field relationships (the buried cone, for example; Clynne and Bleick, 2011; this study), compositional data (Clynne et al., 2000; Clynne and Bleick, 2011), and physical properties of the tephra (this study) show that there were multiple stages to this eruption. Questions motivating this study include:

1. What is the temporal relationship between the tephra eruption and the lava effusion during the Painted Dunes and Fantastic Lava phases of the eruption?
2. What caused the multiple phases of eruption?
3. What is the origin of widespread tephra Unit 3 and why is it so different from that of Unit 2?

This study addresses these questions by concentrating on the physical volcanology of Cinder Cone's tephra deposit. I build on Heiken (1978)'s study of the deposit by analyzing grain size distributions, componentry, and SEM imagery to characterize changes in the nature of the eruptive deposits throughout the tephra sequence. I focus particularly on attempting to relate grain size data, which provide information on the strength of explosive activity, to changes in both bulk composition and groundmass textures, which record conditions of pre-eruptive magma storage.

CHAPTER II

METHODS

2.1. Field Methods

As a baseline, I used recent studies of the distribution and composition of the Cinder Cone tephra deposit by Heiken (1978), Clynne et al. (2000), Clynne and Muffler (2010), and Clynne and Bleick (2011). I have supplemented these studies with data from field campaigns in 2010 (M. Clynne, K. Cashman, and P. Wallace), 2011 (J.K. Marks and K. Cashman), and 2012 (J.K. Marks, M.A. Clynne, P. Wallace, K. Walowski), with the specific goal of understanding the stratigraphic relationships among the different tephra units and sampling the complete stratigraphic section. An additional goal of the 2011 campaign was to trace the spatial distribution of specific eruptive units. In 2012, the goal was to characterize the tephra deposit on and off the lava flows (OB and PD1). Strategies included identifying appropriate places to dig pits to document stratigraphy based on a current topographic and trail map and Heiken (1978)'s isopach map, which was compiled as whole-deposit isopachs by Clynne and Muffler (2010).

Data used in this study come from samples collected from an ~1.2-m-deep pit dug during the first field campaign to the north of Cinder Cone in LAVO (column LCC-1; yellow star in Fig. 2). Ten samples were collected from the top of the column down so as to minimize contamination (sample numbers LCC-1-9 (bottom) through LCC-1-1 (top); Fig. 4). Data from the second campaign include measured thicknesses of the complete tephra section in several locations around the volcano, as well as individual

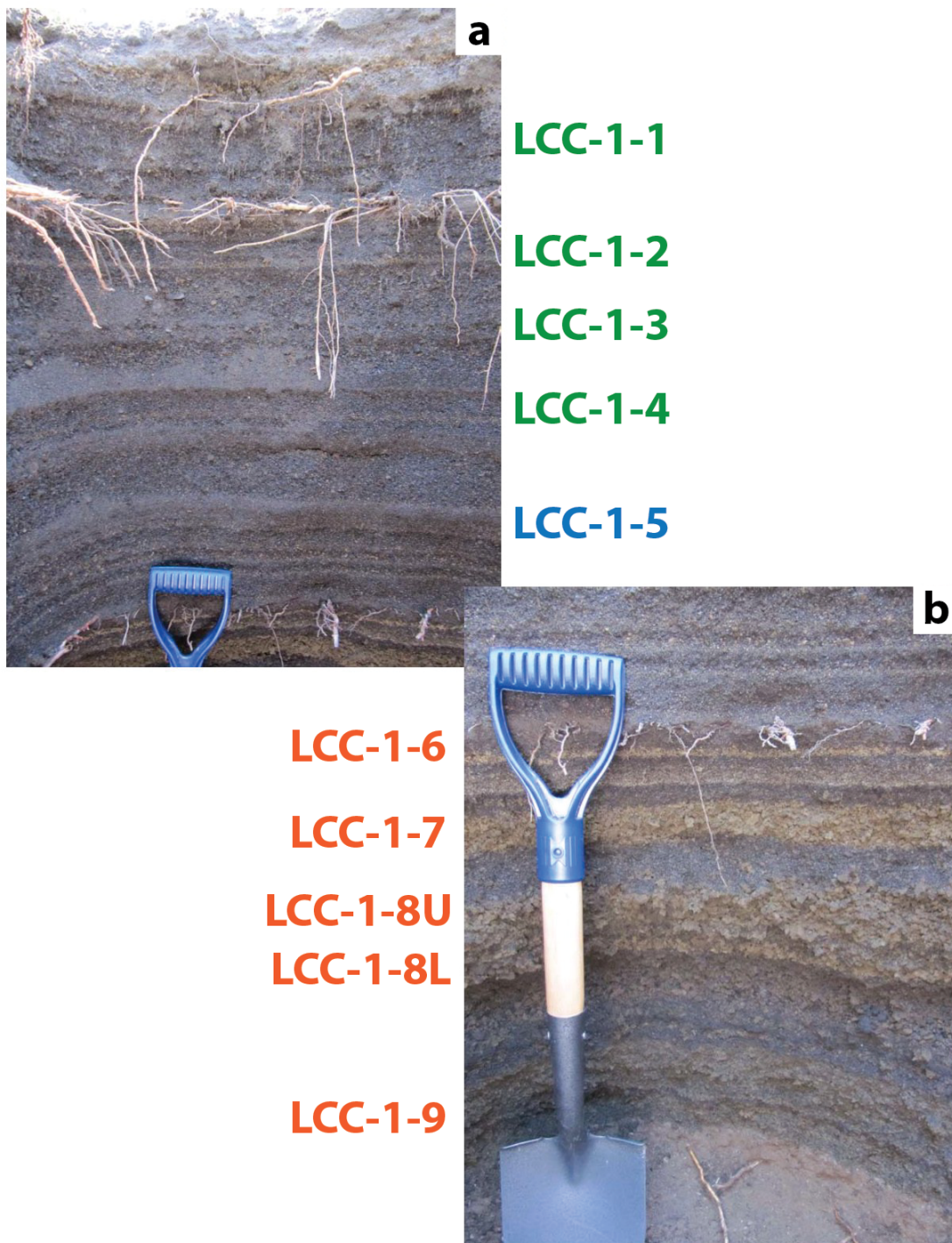


Figure 4. Field photo of the main column, LCC-1, with samples labeled and color-coded by tephra units: Unit 2 = orange, Unit 3 = green, transitional = blue. Colors will be used throughout study. (Photo credit: K. Cashman.)

measurements of Units 2 and 3 (Fig. 5). Observations from the third campaign inform the temporal relationships between the early tephra and lava of Cinder Cone’s eruption.

2.2. Laboratory Methods

Samples were returned to the University of Oregon and dried and weighed before further processing. Grain size distributions were determined using 1Φ sieves ($-5 - 3\Phi$); no wet sieving was performed due to the paucity of very small particles. The mass of each grain size in a sample was summed and compared to the initial mass of the sample in order to estimate error; most final masses were less than their respective initial masses due to particle loss by an average of 3.4 grams, which is an average of 1.3% of the initial mass ($n=10$). Componentry was performed on each grain size interval greater than 1 mm (0Φ). Because of the challenges of working with small clasts, componentry measurements were done only on representative samples of the 0Φ grain size.

Components are based on Heiken (1978)’s original descriptions, although I classified them as golden tephra, black tephra, dense tephra, loose crystals, and other (Table 1, Fig. 6).

Table 1. Descriptions used to perform componentry on grainsize fractions $>1\text{mm}$. See Fig. 6 for a visual comparison of the three main tephra components.

Component	Description
Golden tephra	Highly vesicular and golden or tan in color, with more amoeboid, irregular shapes.
Black tephra	Black, dark brown, or red colored and vesicular. Generally more blocky or smoothly shaped clasts.
Dense tephra	Highly non-vesicular and usually black. Angular. Appearance of small lava chips.
Crystals	Loose crystals - predominantly quartz, but few olivine.
Other	Generally organics, or strange/unknown clasts.

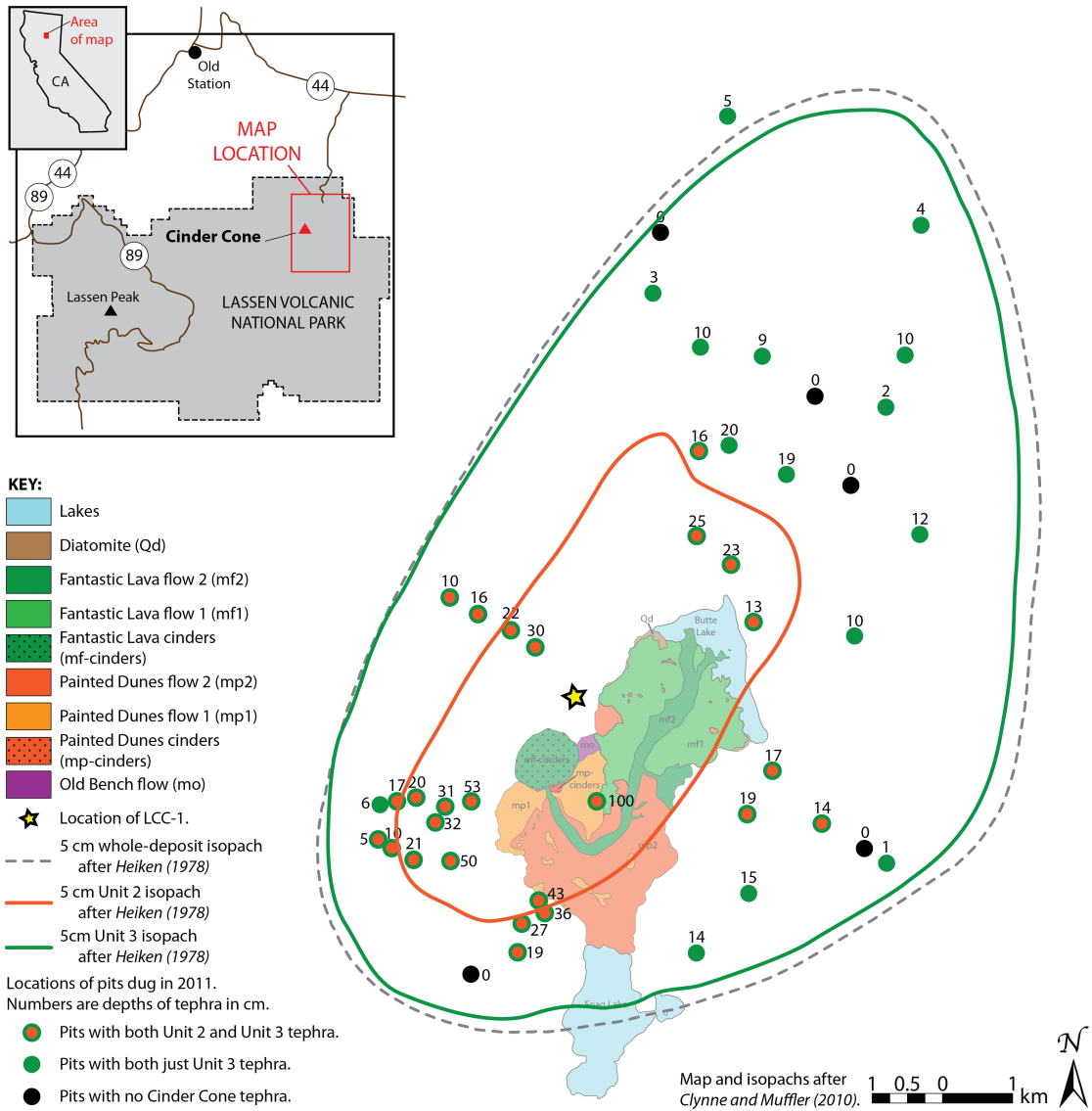


Figure 5. Map highlighting the spatial difference between tephra Units 2 and 3. Isopachs shown are 5-cm isopachs for Unit 2 (orange), Unit 3 (green), and whole-deposit (dashed grey). Dots are locations of individual pits dug in the summer 2011 field campaign and are colored by the tephra units found: orange and green = both Units 2 and 3, green = only Unit 3, black = no Cinder Cone tephra found. Star shows location of column LCC-1, which also contains both Units 2 and 3 tephra. Unit 2 displays a much smaller spatial extent than does Unit 3, which makes up the bulk of the tephra deposit.

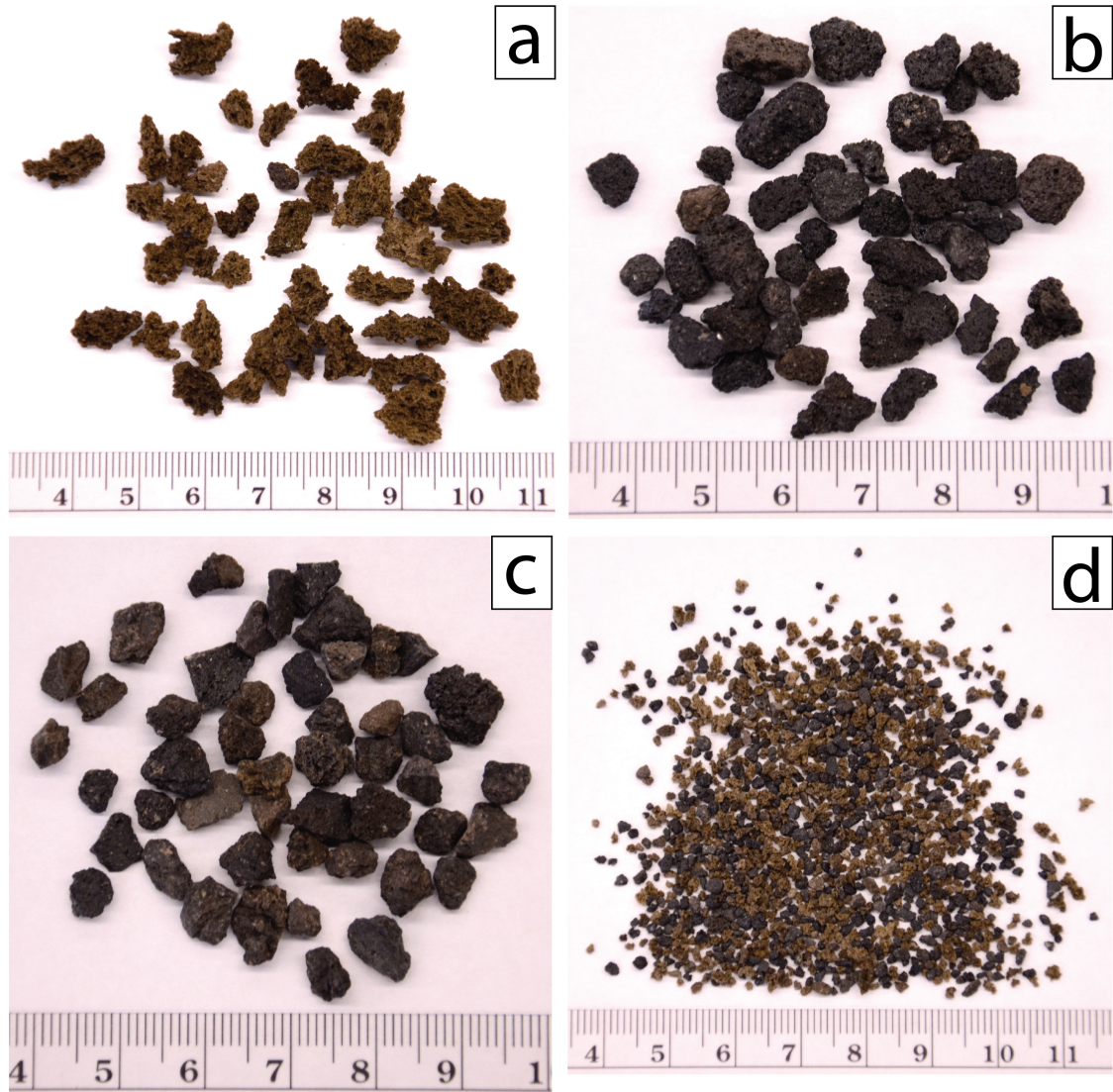


Figure 6. Photos of three main tephra components: a) golden tephra, b) black tephra, and c) dense tephra from sample LCC-1-8U, -2Φ (4-8mm) grain size bin. d) Unsorted tephra from the same sample, but the 0Φ (1-2mm) grain size bin.

Thin sections were created of tephra clasts larger than 16mm from available components for each of the ten samples taken from column LCC-1; multiple clasts were placed on a single slide if possible. High magnification imagery of samples was collected using an FEI Quanta 200 Scanning Electron Microscope (SEM) at the University of Oregon (HV = 15 keV, spot size = 5.0 μm , emission current = 200 μA). Images obtained for analysis spanned multiple areas for each sample (at least 3) and magnifications included 100-150x, 500x, 800x, 1000x, and 3000x to capture a range of vesicle and crystal sizes. Image analysis was performed primarily on golden tephra samples, as they are the easiest to work with (i.e. they contain the fewest crystals). Images were first edited in Adobe[®] Photoshop[®] to clean up charging spots from the SEM, fragments broken off into the vesicles, and cracks. For crystal analyses, each crystal was traced in Adobe[®] Illustrator[®] and the phases were separated and colored in greyscale as follows: vesicles (100% = black), plagioclase (75%), mafics (pyroxene and olivine, 25% = lightest grey), and glass (50%). See Figure 7 for a comparison between an original image and its cleaned and traced image for crystal analysis. All images were then analyzed using ImageJ (Rasband, 2007). Crystallinity values (total, plagioclase, and mafics) are referenced to the total area of all crystals + glass (that is, area percent on a vesicle-free basis).

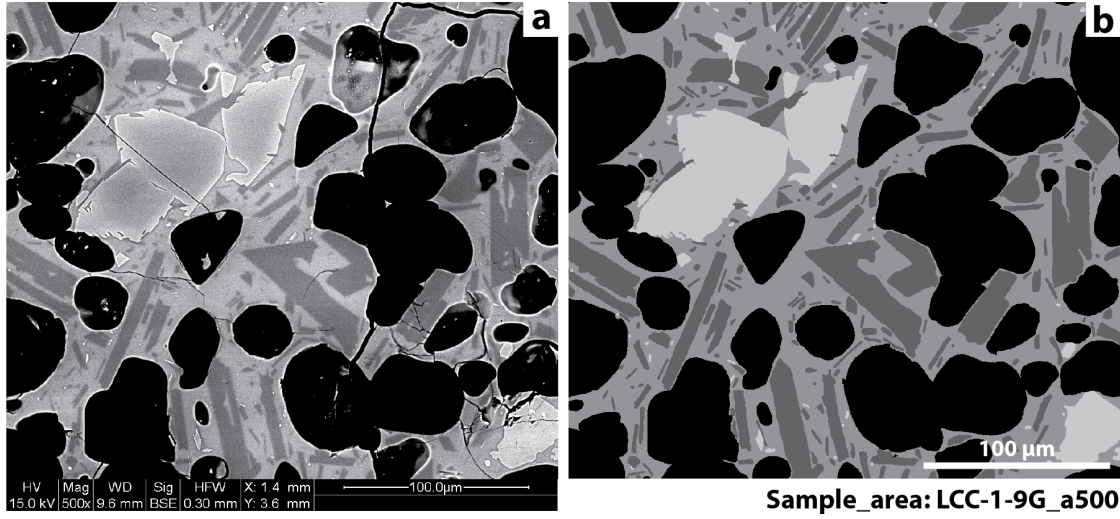


Figure 7. Comparison between the a) original image and the b) cleaned and traced image used in analysis.

CHAPTER III

RESULTS

3.1. Field Results

The main stratigraphic column used in this study, LCC-1, comes from a 1.2-m pit dug north-northeast of the Cone (Figs. 2; 4; 8). The samples were taken from distinctive golden layers throughout the section because these layers were considered most likely to represent primary (rather than reworked/windblown) deposits. Field descriptions of each sample are listed in Table 3 and a corresponding field photo is labeled in Fig. 4.

Table 2. Field descriptions of layers where samples were taken.

Sample Name	Field description of layer
LCC-1-1 [top]	Coarse ash, vaguely laminated with abundant lava chips
LCC-1-2	Tan fine ash layer
LCC-1-3	Two coarse ash layers separated by a thin fine ash layer
LCC-1-4	Two coarse ash layers separated by a thin fine ash layer
LCC-1-5	Fine ash layer that separates Fantastic Lava from Painted Dunes
LCC-1-6	Tan lapilli layer
LCC-1-7	Tan lapilli layer
LCC-1-8U(pper)	[LCC-1-8] Coarse tan lapilli layer, inversely graded. Base has
LCC-1-8L(ower)	abundant oxidized cinder clasts
LCC-1-9 [bottom]	Coarse ash layer with mixed tan and black clasts

The lowermost sample LCC-1-9 comes from a 12.5-cm-thick layer of coarse brown and black ash that is overlain by a 5 cm layer composed of dark coarse ash. Stratigraphically, this lowermost layer could represent either Unit 1 or Unit 2. However, Heiken's (1978) map of Unit 1 suggests that it should be only 10-11 cm thick in this location (which is the maximum thickness Heiken (1978) measured for Unit 1). For this reason I tentatively identify this layer as representing the opening phase of Unit 2.

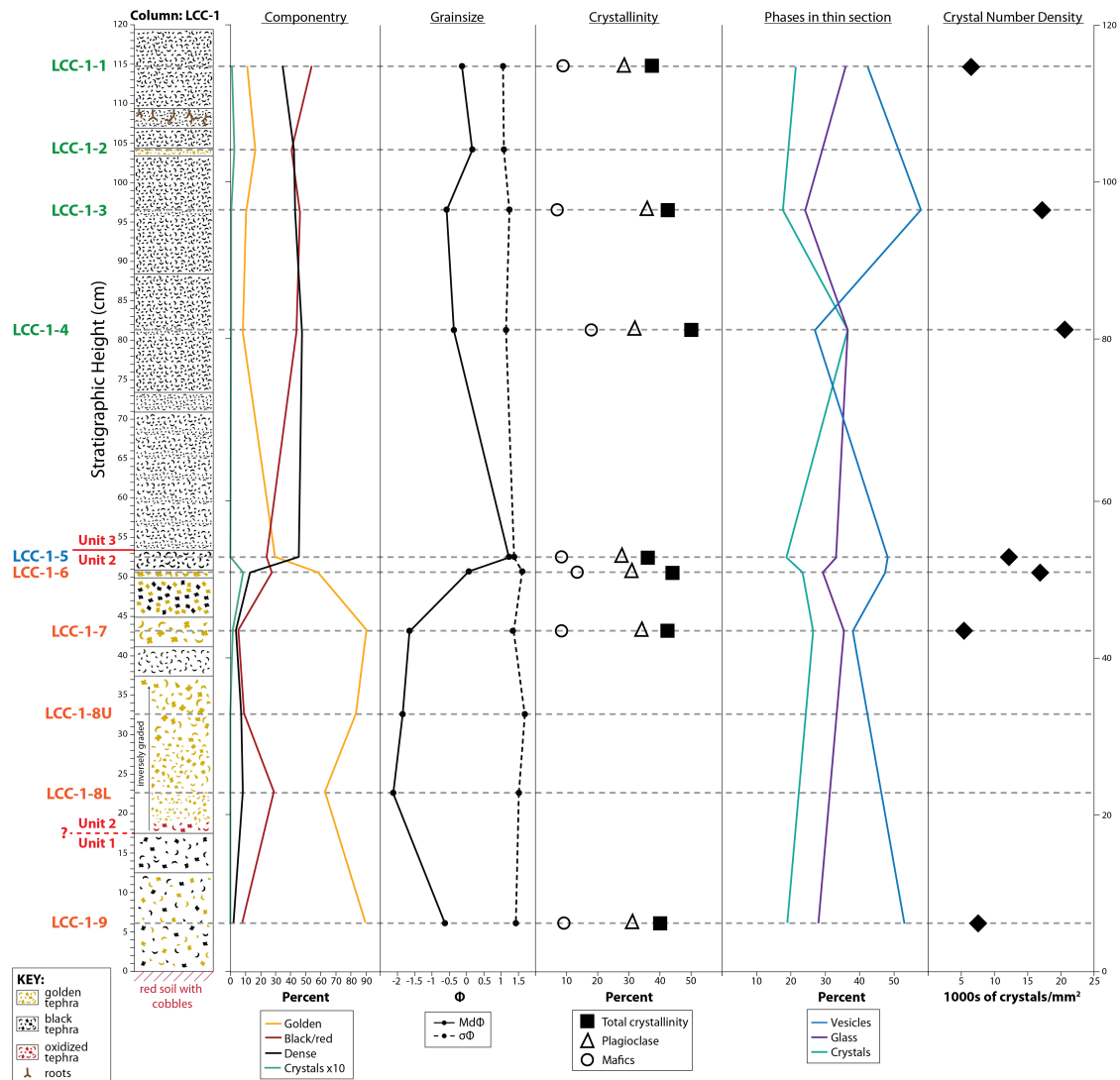


Figure 8. Simplified stratigraphic column shown with data from this study by stratigraphic height. *Componentry* data are from grain sizes greater than 0Φ , though representative samples only were used from the 1Φ bin. Components shown are golden tephra (yellow), black tephra (red), dense tephra (black), and loose crystals multiplied by 10 (green). *Grainsize* data are shown as median diameter ($Md\Phi$) and Inman sorting coefficient ($\sigma\Phi$). *Crystallinity* data are computed by area on a vesicle-free basis and shown for mafic crystals (olivine + pyroxene; open circles), plagioclase (open triangles), and total crystallinity (mafic + plagioclase; filled squares). *Phases in thin section* shows area proportions of vesicles (blue) glass (purple) and crystals (green) in images analyzed for crystallinity. *Crystal Number Density* is computed on a vesicle-free basis and is shown in thousands of crystals per square millimeter.

Samples LCC-1-8L(ower) and LCC-1-8U(pper) come from a 20-cm-thick inversely graded layer of golden lapilli with oxidized clasts at the base. A 3.75-cm-thick dark coarse ash layer with dense clasts overlies this distinct layer. Sample LCC-1-7 comes from a 3.75-cm-thick golden lapilli layer overlain by a 5-cm-thick layer of dark coarse ash intermingled with golden clasts. Sample LCC-1-6 comes from a 1-cm-thick golden lapilli layer. Overlying this thin layer is a 2.5-cm-thick dark fine ash layer from which sample LCC-1-5 comes. This layer was interpreted, in the field, to represent the boundary between tephra Units 2 and 3.

The early phase of Unit 3 includes a 17.5-cm-thick package of alternating cm-scale layers of dark fine and coarse ash, which is overlain by a 2.5-cm-thick dark fine ash layer. The lowermost samples of Unit 3, LCC-1-4 and LCC-1-3, are each from a 15-cm-thick package of two dark coarse ash layers separated by a thin (<1 cm) dark fine ash layer, and a thin (<1 cm) dark fine ash layer separates these two packages. Sample LCC-1-2 comes from a 1-cm-thick golden fine ash layer that overlies the previous samples. Separating LCC-1-2 and LCC-1-1 are two 2.5-cm-thick layers, the lower layer composed of dark coarse ash and the upper layer composed of dark fine ash with abundant roots. The uppermost sample of the column, LCC-1-1, comes from a 10-cm-thick dark coarse ash layer, indistinctly laminated, with abundant lava chips (dense tephra). This final layer of the Cinder Cone eruption is overlain by a thin layer of white 1915 Lassen Peak pumice.

Spatially, Unit 2 is less extensive than Unit 3, particularly in the northeast of the deposit (Fig. 5). With increasing distance from the cone, whole-deposit, Unit 2, and Unit 3 tephra thicknesses all decrease, as does average clast size. Additionally, layering in

both Units 2 and 3, but predominantly in Unit 3, becomes less distinct (Fig. 9). This leaves color and sometimes grain size as unit- or layer-determining factors.

In the field, the OB (Old Bench) and PD1 (Painted Dunes 1) lava flows are both completely covered with up to ~2 meters of tephra (photo a in Fig. 10), including tephra from both Units 2 and 3 (photo b in Fig. 10). The basal layers are welded to the lava and many of the clasts throughout the deposit are oxidized, giving the flows their name. However, there is little tephra to be found on PD2 or FL1 and FL2 (Fantastic Lava) flows, which comprise most of the flow area (Fig. 10). There are also quite a few kipukas (islands) of “painted dunes,” or mounds of lava covered by tephra, in the younger flows (kipukas are labeled as mp1 in mp2 units and as mp2 in mf1 units in Fig. 2).

3.2. Laboratory Results

Grainsize characteristics vary throughout the LCC-1 section (Fig. 8). The median diameter of all samples from column LCC-1 ranges from 1.2 to -2.1 Φ with an average of -0.6 Φ . However, Unit 2 samples (excluding fine-grained sample LCC-1-5) have median grain sizes that range from 0.1 to -2.1 Φ (mean = -1.2 Φ) and are generally larger than Unit 3 samples, where grain sizes range from 0.2 to -0.6 Φ (mean = -0.2 Φ). Thus the grain size changes through the sequence with the largest clasts in Unit 2, an ash layer (Md = 1.2 Φ) at the end of Unit 2/transition to Unit 3, and intermediate clast sizes in Unit 3. All samples are well sorted ($\sigma\Phi$ = 1.1-1.7 throughout the section; mean = 1.4 Φ).

Componentry analysis also shows dramatic changes throughout the section (Fig. 8). Unit 2 samples (numbers LCC-1-9 through LCC-1-6) contain 58-90% golden tephra (mean = 77%), 6-29% black tephra (mean = 16%), 2-13% dense tephra (mean = 7%), and

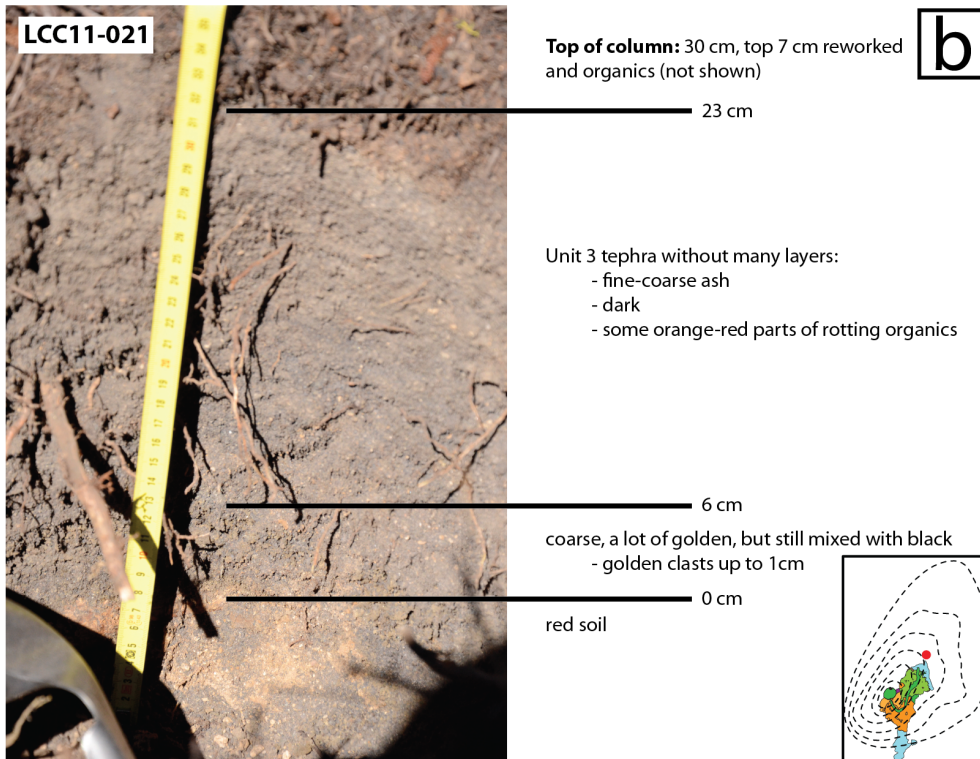
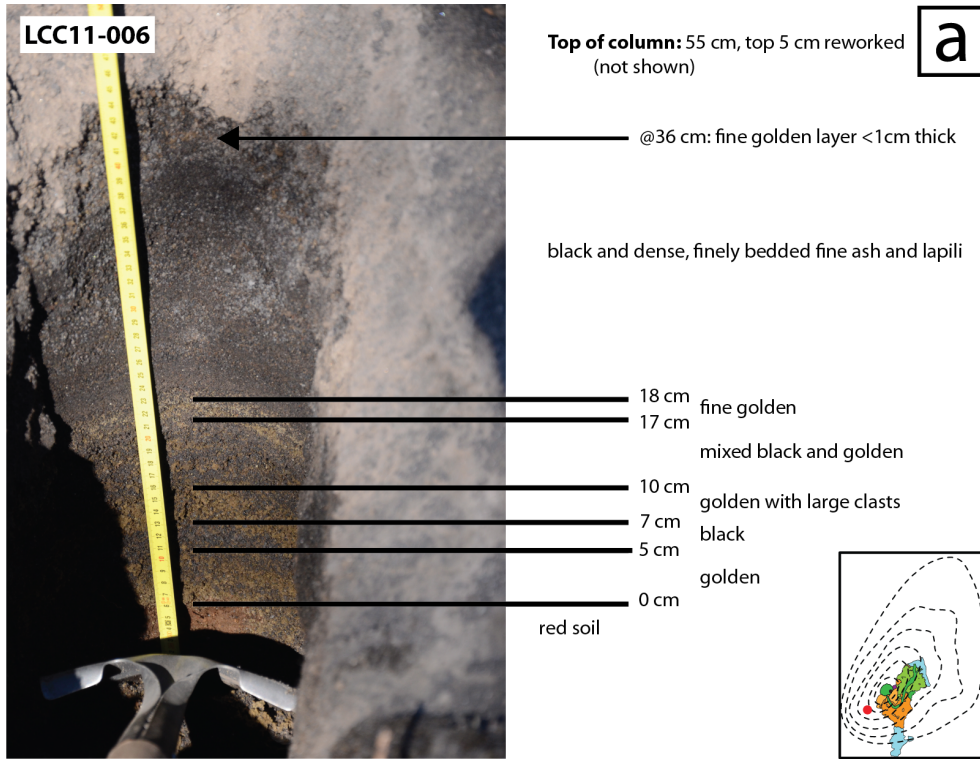


Figure 9. a) Proximal and b) distal field photos of pits dug. Notice the difference in visibility of layering; larger golden clasts are hardly visible at the base of b), but are separated into distinct layers in a).

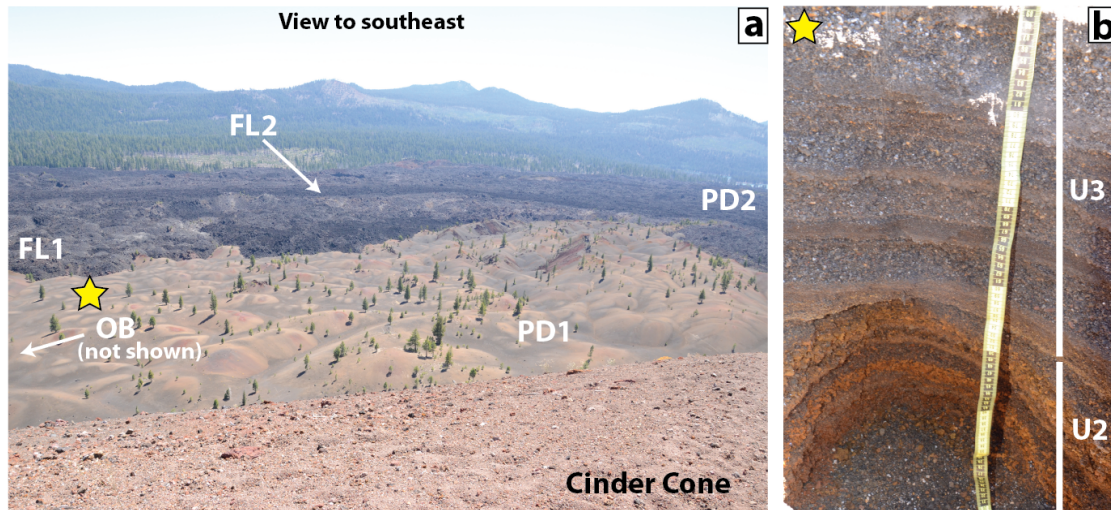


Figure 10. a) Field photo taken from the top of Cinder Cone looking southeast over the Painted Dunes (PD1) and the rest of the lava flows (PD2, FL1, FL2). OB is not shown, though it is also covered with tephra. See Figure 2 for a geologic map. Star shows approximate location of b. b) Field photo of a pit dug on the PD1 flow showing large frothy, but oxidized, clasts and layers of Unit 2 and the darker, finer layers of Unit 3.

0-9% loose crystals (mean = 2.1%). The only apparent trend is an increase in loose crystals from 0-2% in sample LCC-1-7 to ~9% in sample LCC-1-6, right before (perhaps during?) the waning of Unit 2. Transition sample LCC-1-5 has 30% golden tephra, 24% black tephra, 45% dense tephra, and no loose crystals (plus 1% is organics). This layer is distinctive in its dramatic decrease in both golden tephra and loose crystals relative to deposits produced by the main phases of Unit 2. Unit 3 samples contain 8-17% golden tephra (mean = 12%), 41-54% black tephra (mean = 46%), 35-48% dense tephra (mean = 42%) and 0.6-2.8% loose crystals (mean = 1.6%). Again, there are no systematic trends in these data, but the ranges for each component are narrower than in Unit 2 samples (except for dense tephra). Loose crystals reach their maximum of 2.8% in sample LCC-1-2, which also has the most golden tephra of all Unit 3 samples. I have not included percentages for the "Other" component since it contained predominantly recent organics, which are secondary and thus unimportant to this study. Any discrepancies in the sums of percentages are due to organics in the samples.

SEM images show that all tephra types have abundant plagioclase microphenocrysts as well as variable amounts and textures of olivine, pyroxene, and plagioclase phenocrysts (Fig. 11). All samples also contain quartz xenocrysts with variable-width reaction rims (Fig. 12). Visually, golden tephra generally have the smallest amount of microphenocrysts and thus the largest amount of glass. Black tephra have more abundant microphenocrysts as well as quench crystals of plagioclase and pyroxene; the increased crystallinity is probably responsible for the darker color. Dense tephra are almost completely crystalline with very little interstitial glass and few vesicles; crystals are plagioclase and small pyroxenes. See Figure 13 for a visual comparison.

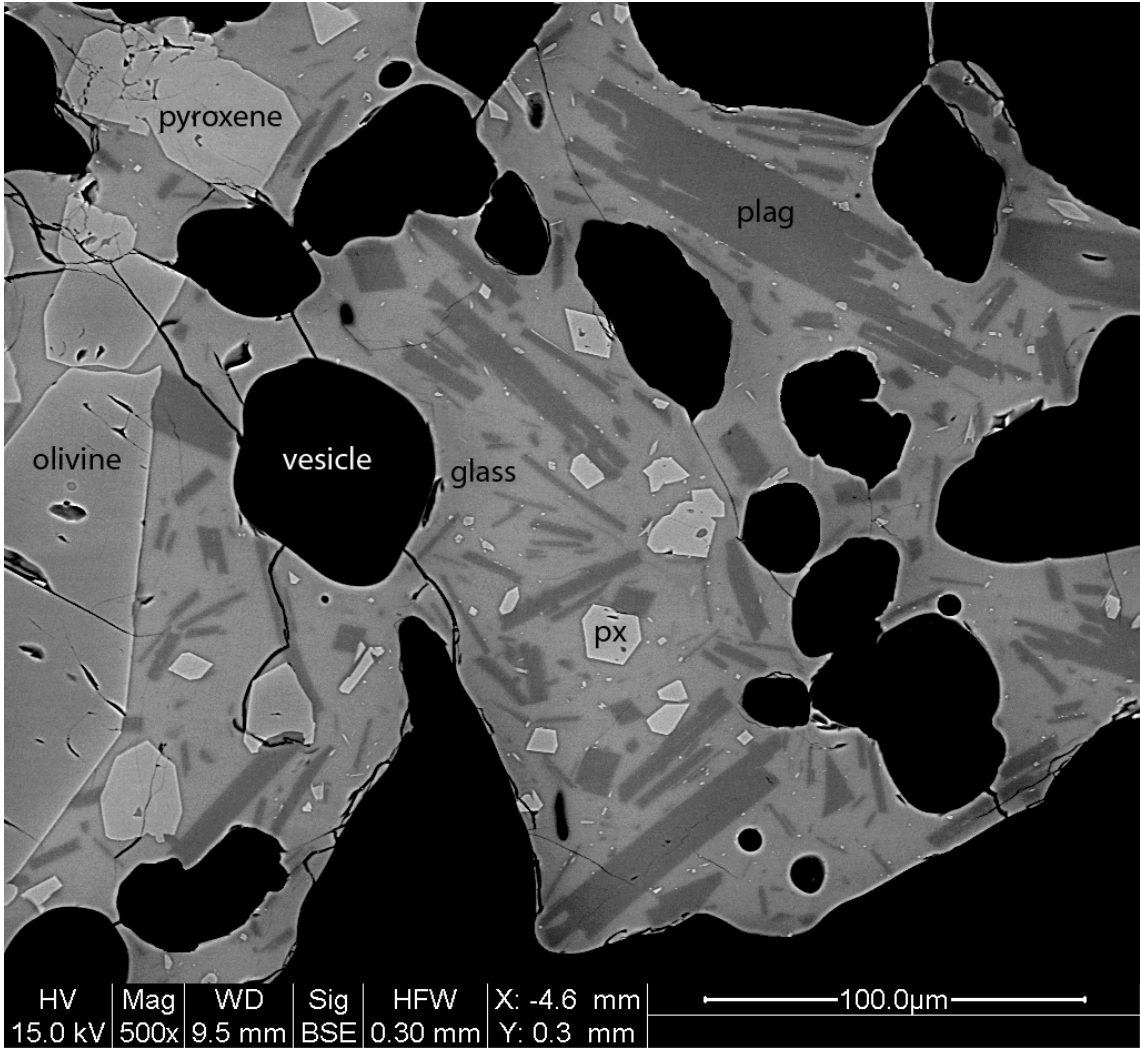


Figure 11. SEM image of sample LCC-1-1G, area a500. Phases are labeled: pyroxene (px), olivine, plagioclase (plag), glass, and vesicle.

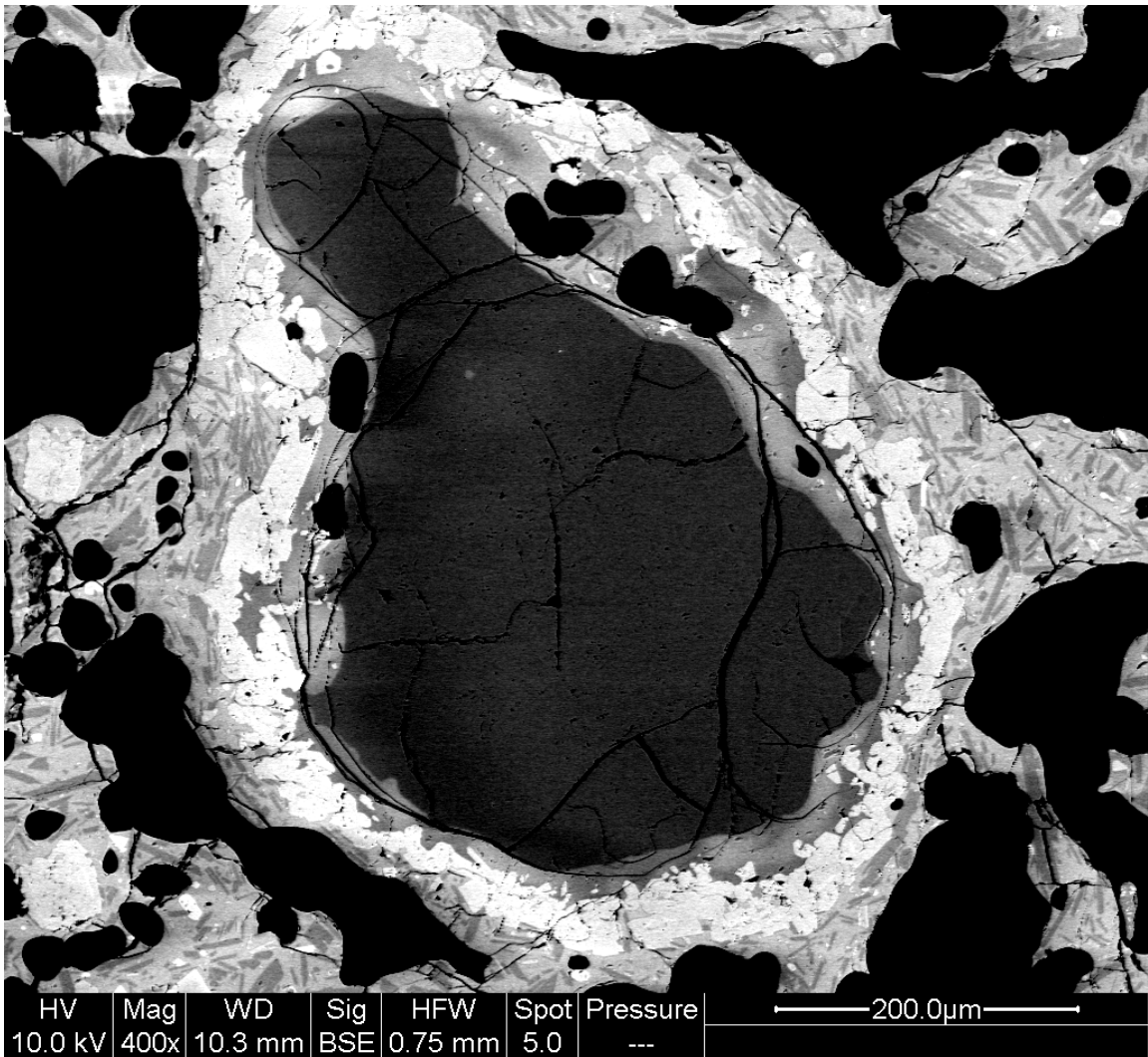


Figure 12. SEM image of a quartz crystal with a pyroxene reaction rim from sample LCC-1-1G, area G1_C400.

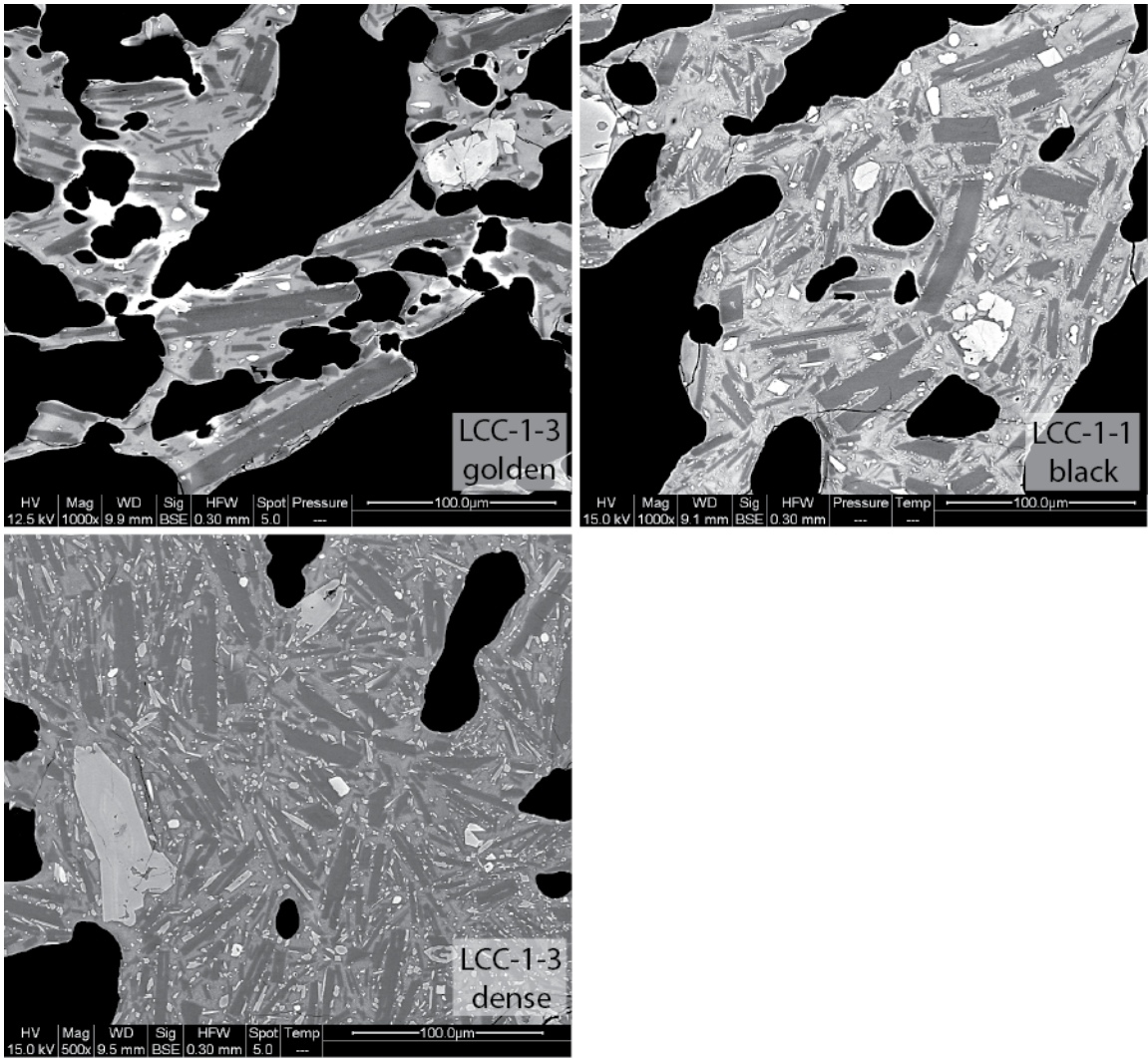


Figure 13. Comparative SEM images of the three components: golden, black, and dense tephra. Scale for each image is 100 μm.

Stratigraphically, individual components do not show much variation. One exception is the golden tephra from sample LCC-1-4, which is striking in the abundance of small plagioclase and mafic crystals (Fig. 14). In our interpretation of the stratigraphy, LCC-1-4 is the lowermost sample of Unit 3, as it lies above the transitional layer (LCC-1-5).

Qualitatively, SEM images show that all tephra types show ranges of vesicle shapes and sizes. Golden tephra have generally the largest and most rounded vesicles. Black tephra have smaller vesicles with amoeboid shapes because of bubble interactions with the abundant microlites. Dense tephra have the fewest vesicles that are also amoeboid in shape. Again, there is little stratigraphic variation in overall vesicle texture within each component, with one exception. The golden component of transition sample LCC-1-5 has much smaller and amoeboid bubbles than do other golden samples and therefore may have experienced some degassing (Fig. 14).

I analyzed crystal sizes and abundance only in the golden tephra (Fig. 8); the black and dense components have a very high groundmass crystallinity that appears secondary (i.e. either quench crystallization or crystallization during recycling and reheating of clasts, or both; Fig. 13). Total crystallinity ranges between 36% and 50%, and increases slightly throughout Unit 2 (from 40% in LCC-1-9 to 44% in LCC-1-6) and then decreases again in transition sample LCC-1-5 (to 36%). In contrast, lowermost Unit 3 sample LCC-1-4 has the maximum crystallinity of all Unit 3 (50%), as well as the whole column, and crystallinity declines steadily throughout Unit 3 to 37% in the uppermost sample (LCC-1-1).

Plagioclase and mafic phases (undifferentiated in image analysis) generally follow the same patterns as total crystallinity, with some notable exceptions. Plagioclase

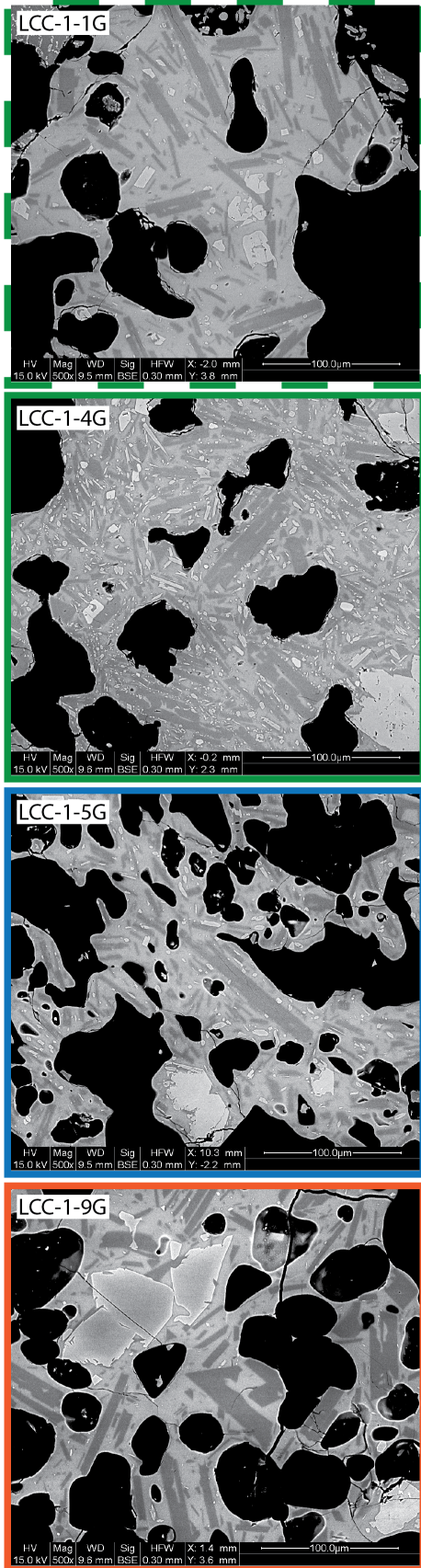


Figure 14. Stratigraphic comparison of SEM images showing a sample from Unit 2 (LCC-1-9G, orange), the transition sample (LCC-1-5G, blue) and two samples from Unit 2 (LCC-1-4G and LCC-1-1G, green). Notice that LCC-1-4G, interpreted here to be the first sample of Unit 3, is highly crystalline compared to the other samples shown. Scale for each image is 100 µm.

crystallinity ranges between 28% and 36% and reaches a maximum in Unit 3 sample LCC-1-3, where mafic content is minimized at 7%. Mafic crystallinity ranges between 7% and 18%, and reaches its maximum value early in Unit 3 (sample LCC-1-4), as does total crystallinity. Within Unit 2, plagioclase reaches a maximum of 34% in sample LCC-1-7, and mafics reach a maximum of 13% in sample LCC-1-6.

Crystal number density (CND; Fig. 8), calculated as the total number of crystals per mm² of bubble free area, ranges between 5,000 and 21,000 crystals per square millimeter. CND is low throughout the beginning of Unit 2 and then spikes before slightly decreasing in the transition sample LCC-1-5 (Unit 2 mean = 9876±6044, LCC-1-5 = 12,000 crystals/mm²). Unit 3 samples show a progressive decrease (mean = 14,645±7301 crystals/mm²) from a high in sample LCC-1-4. CND is minimized toward the beginning of the section (LCC-1-7 = 5366 crystals/mm²), though the lowermost and uppermost samples are also quite low (LCC-1-9 = 7517 and LCC-1-1 = 6431 crystals/mm²), and is maximized in sample LCC-1-4 at 20,398 crystals/mm², the first sample of Unit 3. Both units are highly variable; Unit 2 increases quickly toward the end of the phase, while Unit 3 declines steadily throughout (Fig. 8).

When compared individually, plagioclase CND shows a much narrower range than the mafic crystals do. Plagioclase ranges between 4,000 and 10,000 crystals/mm² while mafics range between 1,000 and 14,000 crystals/mm². Plagioclase is maximized in samples LCC-1-6 and LCC-1-3, which have similar CND values, (9441 and 9614 crystals/mm², respectively) and minimized in sample LCC-1-7 (4,120 crystals/mm²). Mafic crystals are maximized in sample LCC-1-4 at 13,963 crystals/mm², as is total CND. The samples with the lowest mafics CND come from Unit 2 – LCC-1-9 and LCC-

1-7 – though the uppermost sample LCC-1-1 also has a low CND (1,372, 1,247, and 1,866 crystals/mm², respectively). Figure 15 shows histograms of crystal area of all types of crystals counted, split into plagioclase and mafics. The bins with the largest numbers of crystals are the <5 μm² and the 10-50 μm². Notably, the samples that span the Unit 2-Unit 3 transition (LCC-1-6 through LCC-1-3) show larger populations of <5 μm² crystals that are predominantly mafics than do the preceding or following samples. The Rose diagrams show scattered crystal orientations with few preferred directions, except potentially plagioclase in the uppermost samples. Bins plotted at the N-S vectors (and sometimes E-W) hold equant crystals, which are mostly composed of small mafics.

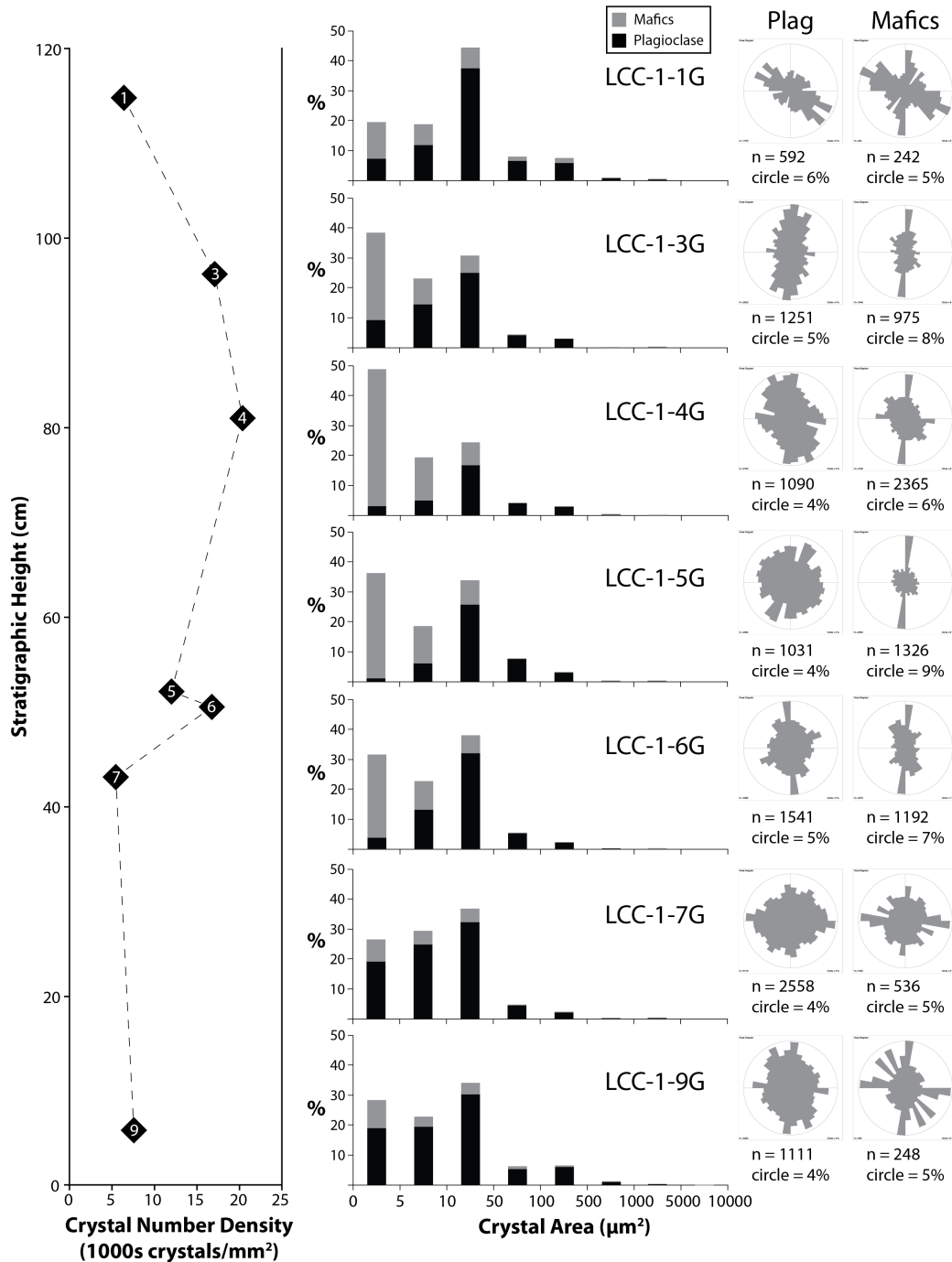


Figure 15. Histograms in percent include all types of crystals but show differences between the percentages of plagioclase (black) and mafic crystals (olivine + pyroxene; grey). Rose diagrams are shown for each mineral/group of minerals. Crystal number density is included as reference. Notably, transitional samples, LCC-1-6 though LCC-1-3 include much larger populations of smaller mafics than do the other samples, particularly LCC-1-4, the first sample of Unit 3. Rose diagrams show some preferred orientations, though the due north, south, east, and west bins hold mostly equant crystals. X and Y axes are the same scale in all histograms, but in the Rose Diagrams, the circle is variable between 5 and 6%.

CHAPTER IV

DISCUSSION

The objective of this study is to infer details of Cinder Cone's eruption using the physical characteristics of its tephra deposit. I have built on initial studies by workers such as Diller (1851) and Heiken (1978) and have augmented my data with compositional and geochemical data from collaborative workers. This work is important for understanding the range in eruptive styles and mechanisms of cinder cone volcanoes and for assessing the hazards posed by future Cascade eruptions. Goals initially posed in this study include describing and understanding the temporal relationship between the tephra and lava eruptions, as well as the origin of the different tephra units and lava flows. First, I will summarize and interpret the data and compare Cinder Cone characteristics to other studied eruptions and deposits. Second, I will briefly describe geochemical data and results, and how these data tie in to Cinder Cone's eruptive progression. Finally, I will describe my interpretation of Cinder Cone's eruptive styles.

4.1. Deposit Characteristics

Physical data on explosive deposits provide information about eruption style and explosivity. Data and interpretations presented in this section (spatial distribution, field observations, grain size characteristics, and componentry) all relate to how the volcano erupted and by what mechanism. In this section, I summarize the data on tephra characteristics and compare Cinder Cone to observed and described other mafic eruptions. An important caveat to remember about the tephra samples is that the ten

samples in this study come from specific layers of the deposit (Fig. 4) and not from a centimeter by centimeter sampling. The goal of this sampling was to obtain the most pristine samples to work with, but will have biased the results because the samples come from layers of different thicknesses, which represent different time spans.

4.1.1. Spatial distribution of eruptive units

The volume and spatial extent of tephra deposits provides important information about the explosivity of an eruption since eruptions with small volumes and areal coverages are generally less explosive (e.g. McKay, 2012). As described by Heiken (1978), Unit 1 of the tephra is insignificant, both in volume and spatial extent. Using previously collected isopach data, I have calculated the areal extent of Unit 2 as $\sim 40 \text{ km}^2$ at the 5-cm isopach whereas that of Unit 3 is $\sim 100 \text{ km}^2$ (Fig. 16; Heiken, 1978). Previous workers estimated the volume of Cinder Cone's eruptive products to be 0.36 km^3 dense rock equivalent (DRE), of which, 88% is lava and 12% is tephra (Clynne and Bleick, 2011). By these numbers, the volume of lava is $\sim 0.32 \text{ km}^3$ DRE and the volume of tephra is $\sim 0.04 \text{ km}^3$ DRE.

To build on previous work, I calculated the volume of individual tephra units using the isopach maps (e.g. Fig. 5) from Heiken (1978) and the method of Pyle (1989). This method uses a plot of the logarithm of (isopach) thickness versus the square root of isopach area to estimate deposit volume (Fig. 1) under the assumption that the deposit displays exponential thinning, which creates a linear trend. Accurate calculations require detailed sampling of both the proximal and distal portions of the deposit. Additionally, many deposits deviate from the simple exponential decay because of depositional or

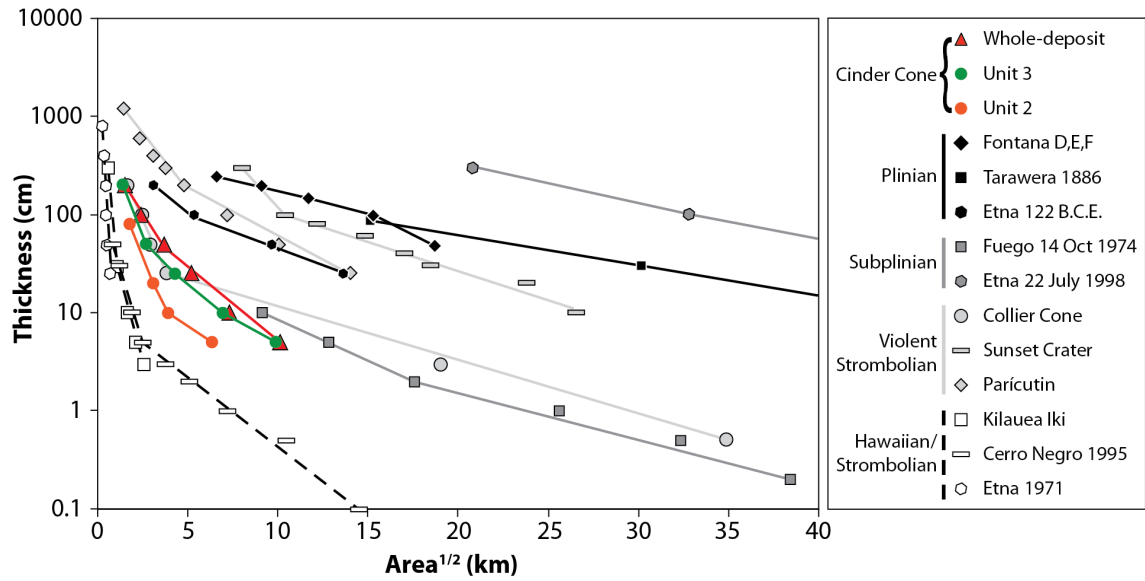


Figure 16. A thickness versus square root of area isopach plot after Pyle (1989) showing the spatial differences between Units 2 and 3 as well as other cinder cone and basaltic explosive data. Unit 2 has a strongly negative slope similar to Hawaiian eruptions, but it has a greater area than other less explosive deposits. The proximal slope of Unit 3 mimics that of a cinder cone in the Cascades (Collier Cone). References are the same as Figure 1.

erosional processes. I have calculated that the volume of Unit 2 tephra is $\sim 0.06 \text{ km}^3$ and that of Unit 3 is $\sim 0.15 \text{ km}^3$, for a total minimum tephra volume of $\sim 0.21 \text{ km}^3$, or 0.13 km^3 DRE (at 40% vesicularity, as previously used in Clynne and Bleick, 2011). This volume estimate is a minimum because I do not have data on the distal portions of the deposit, which have probably been weathered and eroded away.

To obtain a complete picture of the erupted volume, material comprising the cone must be added to the volume of the tephra and lava. I estimated the cone volume using the method of Kervyn et al. (2012), who assume a simplified form of an axi-symmetric truncated cone on a flat surface with an inverted cone representing the crater. The parameters I used are: diameter of the cone (W_{co}) = 978m; height of the cone (H_{co}) = 213m; diameter of the crater (W_{cr}) = 301m; depth of the crater (D_{cr}) = 53m (measured via google Earth™). The calculated cone volume is 0.44 km^3 , or 0.26 km^3 DRE. The addition of the cone increases the total volume of explosively erupted material to $\sim 0.39 \text{ km}^3$ DRE, considerably greater than previously estimated for the tephra deposit (0.04 km^3 DRE).

Finally, I estimated lava flow volume to obtain a total volume estimate for the whole eruption. Using an average thickness of 25m (minimum estimate from topographic maps) and an area calculated using digital maps on ArcGIS, my calculated lava flow volume is 0.19 km^3 (assumed DRE), considerably less than published estimates. Potential problems with my calculation include the generalization of lava flow thickness as well as uncertainty in knowing the exact base of the flows. This large discrepancy must come from differences in measured values for thickness and area, and calculation methods. To make up the entire difference using only flow thickness would require that the flows average 40m thick, which is plausible for small areas, but not over the whole flow. Using

my lower lava flow volume estimate, the total calculated volume of the Cinder Cone eruption is 0.58 km³ DRE, of which 33% is lava flows and 67% is explosive material (45% is cone and 22% is tephra). Using the previous estimate of 0.32 km³ for the volume of the lava flows and my estimates for the cone and tephra, the total calculated volume of Cinder Cone is 0.71 km³, of which 45% is lava flows and 55% is explosive material (37% is cone and 18% is tephra).

A comparison of the spatial extent of the deposits of individual Cinder Cone units with those of other well-characterized mafic eruptions can be used to place these eruptions in a wider context. The Unit 2 deposit is slightly thicker and more widespread than deposits of Kilauea, Hawaii, Cerro Negro, Nicaragua, and Etna 1971, Italy, which are classified as Hawaiian and Strombolian eruptions (Fig. 16). In contrast, the spatial distribution and thickness of Unit 3 as well as the whole tephra deposit more closely resemble those deposits of Fuego volcano in 1974, as well as that of the c. 1500ybp eruption of Collier Cone, OR, which have been classified as subplinian and violent Strombolian eruptions. Even thicker and more widespread are deposits of other violent Strombolian and basaltic Plinian eruptions such as Parícutin and Sunset Crater (Arizona), and Tarawera 1886. Therefore, while there are differences between Units 2 and 3, Unit 3 tephra dominates the deposit and the total thickness and spatial extent indicate a moderately explosive eruption style. I note that this study lacks data about the distal Cinder Cone deposit and I expect that the finest grained and most widespread component of the tephra deposit is probably missing from the record due to weathering and erosion.

4.1.2. Sequence of events

Previous work indicates that Cinder Cone erupted in three phases that included both explosive and effusive styles (Heiken, 1978; Clynne et al., 2000; Clynne and Bleick, 2011). According to bulk rock geochemical data, the tephra and lava compositions display similar variation throughout the eruption (Fig. 3). Therefore it has been assumed that the tephra units correspond with and were erupted around the same time as the lava flows: Unit 1 tephra has been linked with the Old Bench flow, Unit 2 tephra with the Painted Dunes flows, and Unit 3 tephra with the Fantastic Lava flows.

One test of the relationship between the tephra and lava units is to examine the tephra preserved on the lava flow surfaces. The OB and PD1 flows are covered with thick tephra deposits (Fig. 10a); the blanketing tephra is also oxidized by contact with hot flows. In contrast, there does not appear to be tephra deposition on the later flows (PD2, FL1, and FL2). It is possible that there may be tephra hidden within the brecciated surface of these flows. However, these flows contain kipukas of tephra-covered mounds (one such kipuka is visible in the background of Fig. 10a) that appear to be earlier lava flows covered by tephra (e.g. OB or PD1), although they could be sections of rafted cone material. Taken together, it appears that the tephra-producing phase of the eruption may have ended prior to eruption of PD2.

To test this hypothesis, I dug pits on OB, PD1, and off the flows proximal to OB to determine the relative relationships between the tephra emission and early lava flow effusion (PD1 pit location in Figs. 5, 10a; OB and off flow pit locations in inset map of Fig. 17). It is easy to distinguish tephra units and layers without extensive laboratory analysis because tephra from Units 2 and 3 is distinctive in the field (e.g. Fig. 4). Unit 2

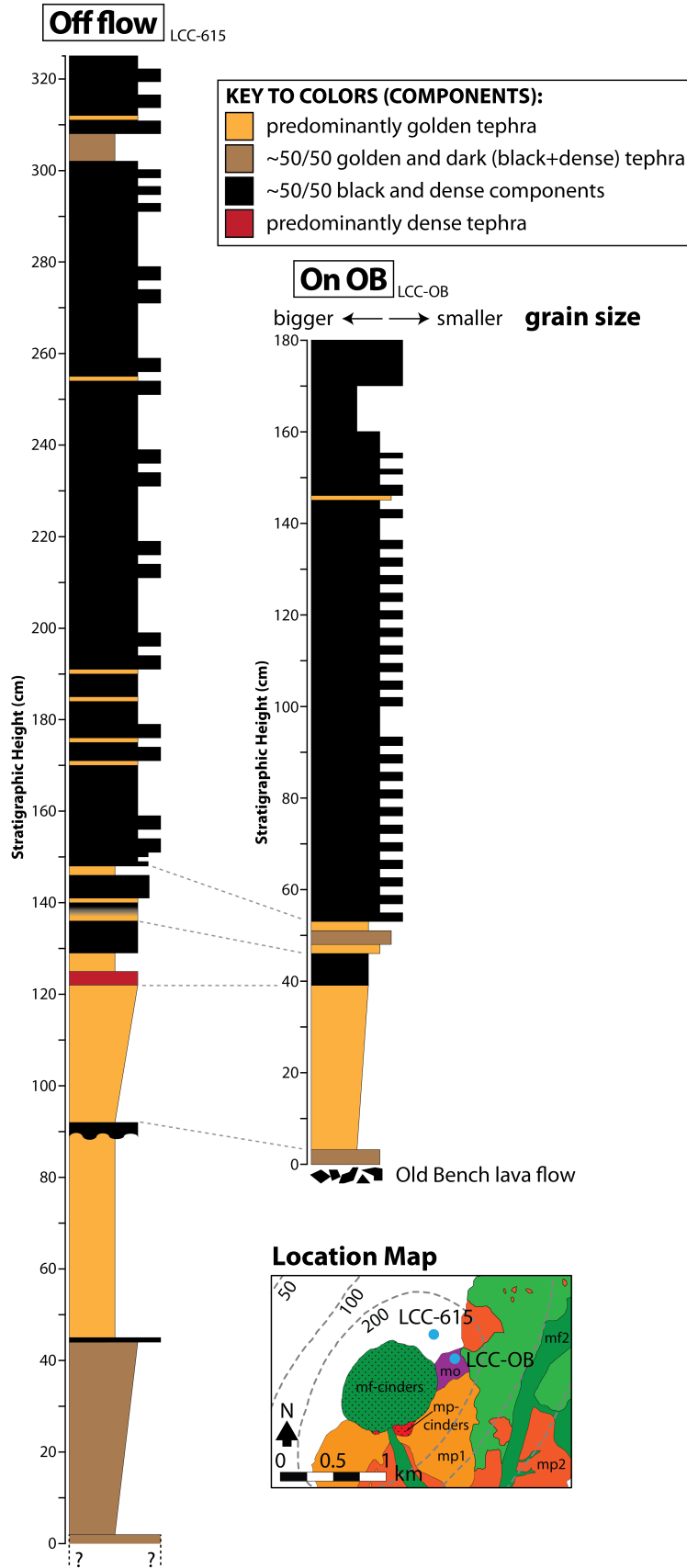


Figure 17. Schematic stratigraphic columns of pits dug off flow (LCC-615) and on top of Old Bench (LCC-OB).

layers are dominated by golden tephra and the clasts are generally larger (Figs. 4, 9, 10b) whereas Unit 3 tephra is composed predominantly of black and dense tephra clasts that are generally smaller. Proximally, Unit 3 layers are also very cyclic, alternating between fine lapilli and coarse ash layers regularly up section. Distally, these layers disappear, probably due to secondary processes. The transition between Units 2 and 3 is sometimes defined by a thin, fine ash layer that separates the bulk of the golden tephra-dominated layers from the cyclic darker tephra layers. This thin layer is found in the main column of this study as sample LCC-1-5.

The pit dug on OB reached the lava flow after 180 cm, which lay just below a red- and purple-oxidized coarse ash layer (see schematic column in Fig. 17). We interpret this basal oxidized layer to be Unit 2 tephra as it is overlain by a thick layer of large golden clasts. This distinctive layer was overlain by a layer of larger black and dense tephra clasts and the uppermost layers of Unit 2 were two layers golden tephra layers separated by a layer with a higher proportion of dark tephra. Unit 3 in this location was composed of ~25 couplets of alternating fine and coarse ash layers. The pit dug on PD1 was ~100 cm thick, though we did not reach the lava flow. The lowest layer that we observed contained large, oxidized golden tephra clasts, and this layer appears to be the same distinctive layer observed on OB (Fig. 10b). Unit 2 ended at a layer of golden lapilli and Unit 3 again shows repeating, dark, fine and coarse ash layers. The pit located just off the flows was over 3 meters thick and we did not reach the base of the tephra. The base of the section is composed of approximately equal proportions of golden and dark tephra, which I suggest are similar to sample LCC-1-9 of this study (Fig. 17). The bulk of Unit 2 comprises two thick layers of predominantly large, golden clasts; I suggest that the upper

layer is the same thick golden layer that exists on OB and PD1. Around the Unit 2-Unit 3 transition, there are three thin layers of golden coarse ash that probably correspond to the two thin golden layers on OB. Above the transitional area, Unit 3 again shows cyclic changes in grain size while staying predominantly black and dense tephra. There are uncommon, thin golden layers interspersed throughout Unit 3.

Based on these exploratory pits, I can narrow down the timing and deposition of the early phases of the eruption. First, we have not found a convincing sample of Unit 1 as described in Heiken (1978). Second, both the OB and PD1 flows were emplaced during the Unit 2 tephra emission since there exists only one thick layer of large golden clasts on both of the flows and two thick layers of large golden clasts directly off of the OB flow. The OB flow probably erupted in the time between those two golden layers since the tephra directly overlying the lava is darker coarse ash. The PD1 flow must have been emplaced after because it overlies OB, but the PD1 pit contained most of the same tephra layers as the OB pit. This suggests that they were erupted at very similar times in the sequence, or at the latest during the middle of the emission of the upper large golden layer. Finally, as has been mentioned, the tephra directly on top of both lava flows is oxidized red, purple, and orange, indicating that the lava was still hot as the tephra was deposited. This observation contradicts previous eruption sequences that place OB and PD1 in separate phases, and suggests that OB and PD1 are nearly contemporaneous with each other and with Unit 2. It is difficult, however, to constrain Unit 3 in relation to the lava flows since there is no visible tephra on the PD2, FL1, and FL2 lava flows.

4.1.3. Grain size characteristics

Deposit grain size data are useful because they provide information regarding the explosivity of an eruption. One way to display and compare grain size data is on a plot of median diameter ($Md\Phi$) vs. the Inman sorting coefficient ($\sigma\Phi$; Fig. 18). This plot is useful because different eruption styles tend to cluster in different areas of the plot. It is important to note that these types of data are typically shown for a single location (i.e. all samples from a single stratigraphic section) and not for the entire deposit. Grain size data change with distance away from vent, so results can be skewed if samples from different eruptions come from different distances from the vent.

The data shown in Figure 18 come from a single location and therefore describe changes in the temporal sequence of the eruption, without providing comprehensive information on the spatial variations in grain size data. All samples are well sorted, indicating deposition as pyroclastic fall deposits. Samples from Unit 2 are the largest of the section and plot in the center of the Strombolian field. Transition sample LCC-1-5 is has the smallest median size and plots in the center of the violent Strombolian field. Unit 3 samples generally have median sizes that lie between the largest and smallest samples of Unit 2 and plot in the violent Strombolian field. Grain size data for the Cinder Cone samples are similar to those of Parícutin in Mexico as well as Lava Butte in Oregon, which are classified as violent Strombolian eruptions.

4.1.4. Deposit components

Quantifying the component abundance and characteristics is important for determining near-surface and eruptive mechanisms. Clasts are separated into components

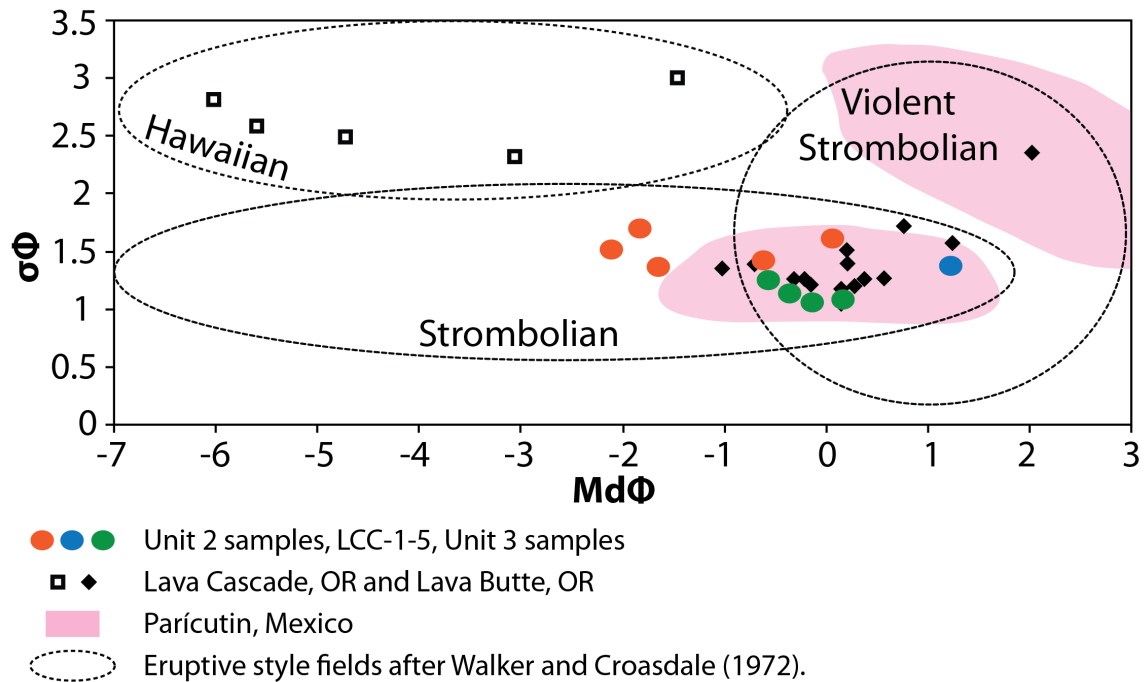


Figure 18. A median diameter versus sorting (both in Φ units) plot highlighting the differences between Units 2 and 3 of Cinder Cone as well as other cinder cone eruptions. References: Lava Cascade and Lava Butte, *D. McKay, pers. comm.*; Parícutin, *Pioli et al. (2008)*.

based on color, vesicularity, and morphology and combined with detailed SEM analysis to infer ascent processes. Componentry data are displayed on a ternary plot of the three main component types – golden, black, and dense tephra – which excludes loose crystals and other clasts/debris (Fig. 19). Plotting data on this ternary diagram reveals trends and fields that correspond to the temporal evolution of eruption style.

As seen in the deposit distribution and grain size characteristics, the components vary dramatically between Cinder Cone tephra Units 2 and 3 (Fig 8). Unit 2 is dominated by coarse, frothy golden tephra, while transition sample LCC-1-5 and Unit 3 are dominated by black and dense tephra. When compared with other eruptions, three Unit 2 samples have similar componentry to the opening phase of the Kilauea Iki eruption in Hawaii, which is classified as a Hawaiian-style eruption (Fig. 19). Other Cinder Cone samples, including two Unit 2 samples, the transition sample, and all Unit 3 samples, contain larger quantities of dense tephra than do most of the samples from Lava Butte, OR and Parícutin, Mexico, though the final phase of the eruption of Parícutin overlaps with Unit 3 samples (Fig. 19). These eruptions have been classified as violent Strombolian eruptions. Interestingly, Parícutin follows a temporal trend similar to that of Cinder Cone in which the proportion of dense clasts increases throughout the eruption, while Lava Butte samples mostly remain on the golden-black spectrum. Cinder Cone is different from both Lava Butte and Parícutin because of the distinctiveness of the different tephra units; Lava Butte and Parícutin both seem to grade between proportions of components during the phases, but Cinder Cone shows wholly distinct phases. Therefore, Cinder Cone erupted by at least two different eruption styles, a less explosive Hawaiian-like style and a more explosive violent Strombolian-like style. These eruptions

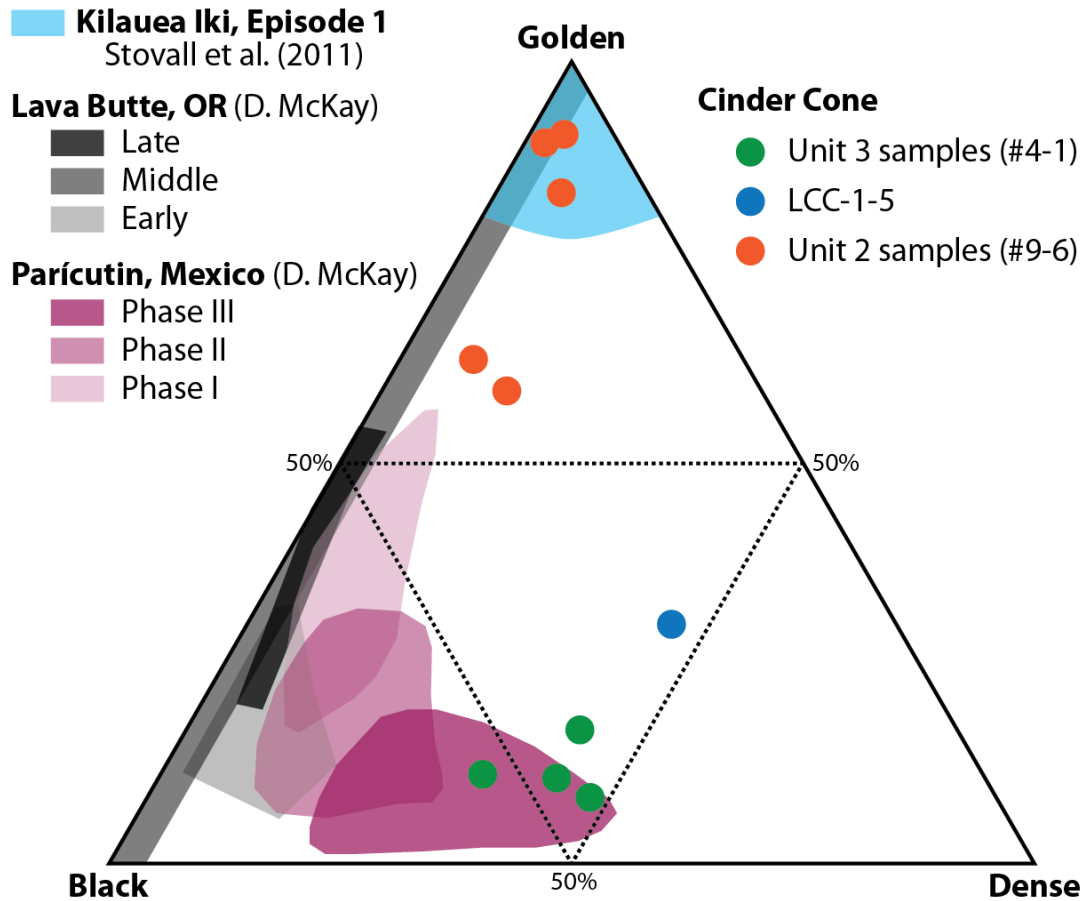


Figure 19. Componentry data of Cinder Cone and other mafic cinder cone volcanoes. References: Kilauea Iki, HI, USA, *Stovall et al. (2011)*; Lava Butte, OR, USA, *D. McKay, pers. comm.*; Parícutin, Mexico, *Pioli et al. (2008)*.

are distinct in their componentry, signifying the involvement of another process (e.g. eruptive pause or new magma batch).

4.2. Textural Analysis

Crystal textures provide information on eruptive and pre-eruptive magmatic processes (e.g. transport and storage). For example, variations in crystal number density with crystallinity can be used to distinguish nucleation-driven crystallization from growth-driven crystallization (Hammer et al., 1999; Fig. 20). If crystallization is nucleation-driven, then the number of crystals will increase significantly without much of an increase in crystallinity, since the crystals remain small. If crystal growth is the dominating process, crystallinity of the clast will increase without a significant increase in crystal number density. This distinction is important because nucleation-dominated crystallization trends can be used to infer variations in rates of magma ascent.

Plagioclase abundance is generally 28 to 36%, with measured number densities of 4.1 to 9.6×10^3 crystals/mm² (Fig. 21). The lack of significant variation in plagioclase textures indicates mostly constant crystallization conditions during magma ascent that were dominated by plagioclase growth. In contrast, mafic crystals are less abundant (7 to 18 vol %), and have more variable crystal number densities (1.2 to 14.0×10^3 crystals/mm²). This variation suggests that the magma underwent dynamic processes that initiated the nucleation of mafic crystals without allowing for their growth. That different processes acted on different minerals implies variations in magma transport. I used the program MELTS to create a phase diagram for the Cinder Cone composition listed in Table 3 (Fig. 22; Ghiorso and Sack, 1995; Asimow and Ghiorso, 1998). This phase

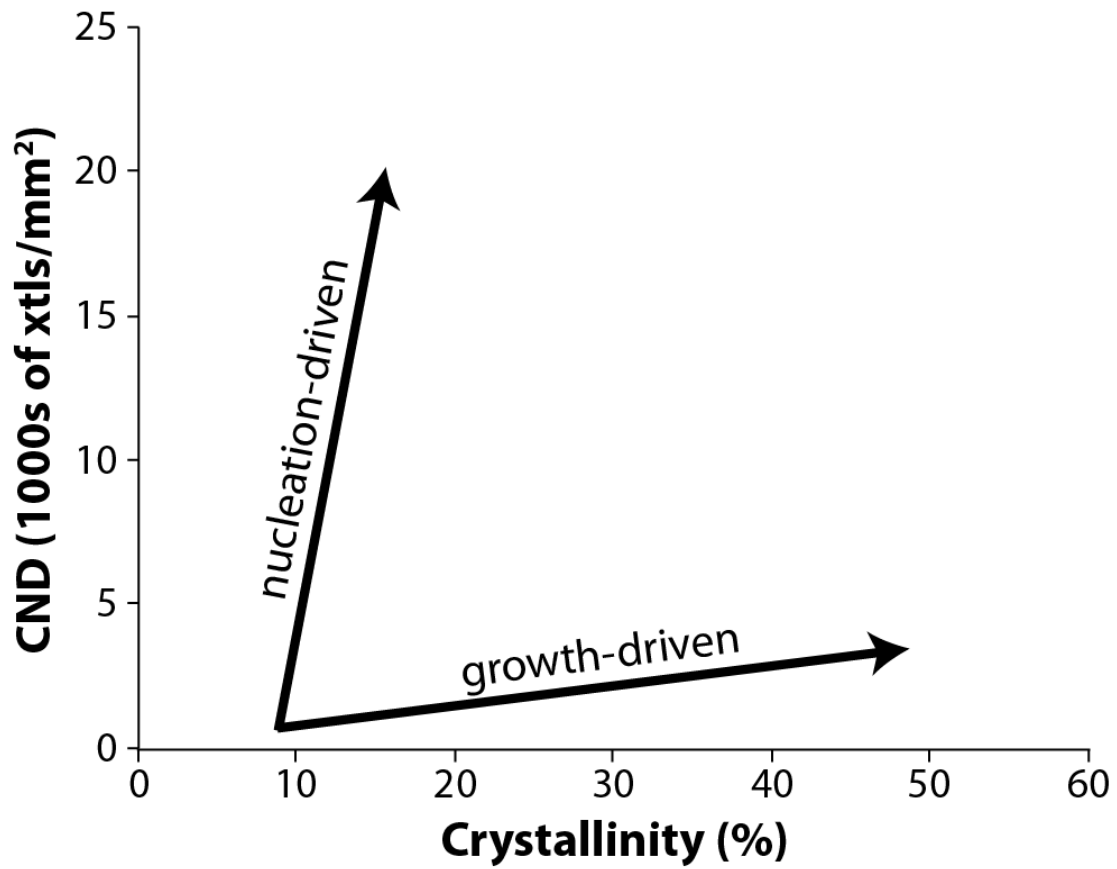


Figure 20. Schematic plot of crystallinity versus crystal number density showing expected trends for different dominating processes during the ascent of magma.

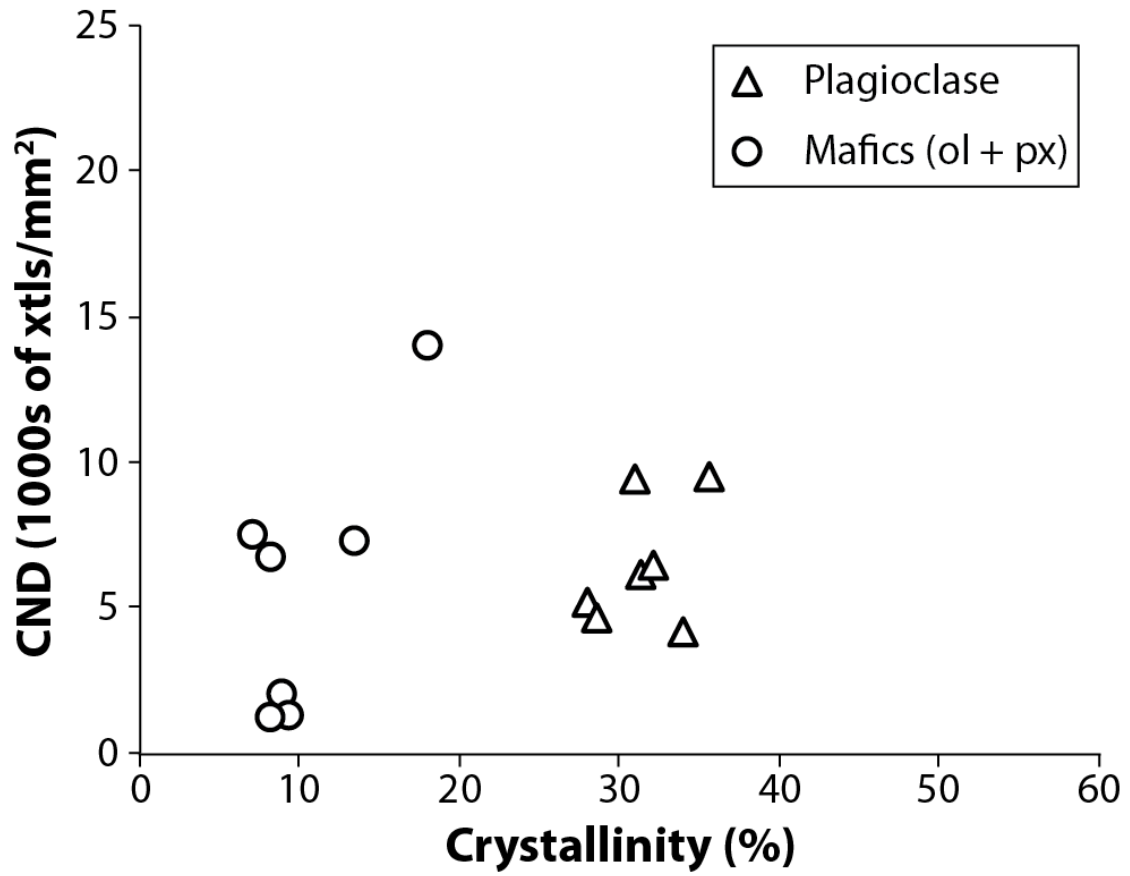


Figure 21. Crystallinity plotted against crystal number density for mafic crystals (olivine + pyroxene) and plagioclase. Plagioclase crystals are clustered, indicating constant crystallization conditions during ascent.

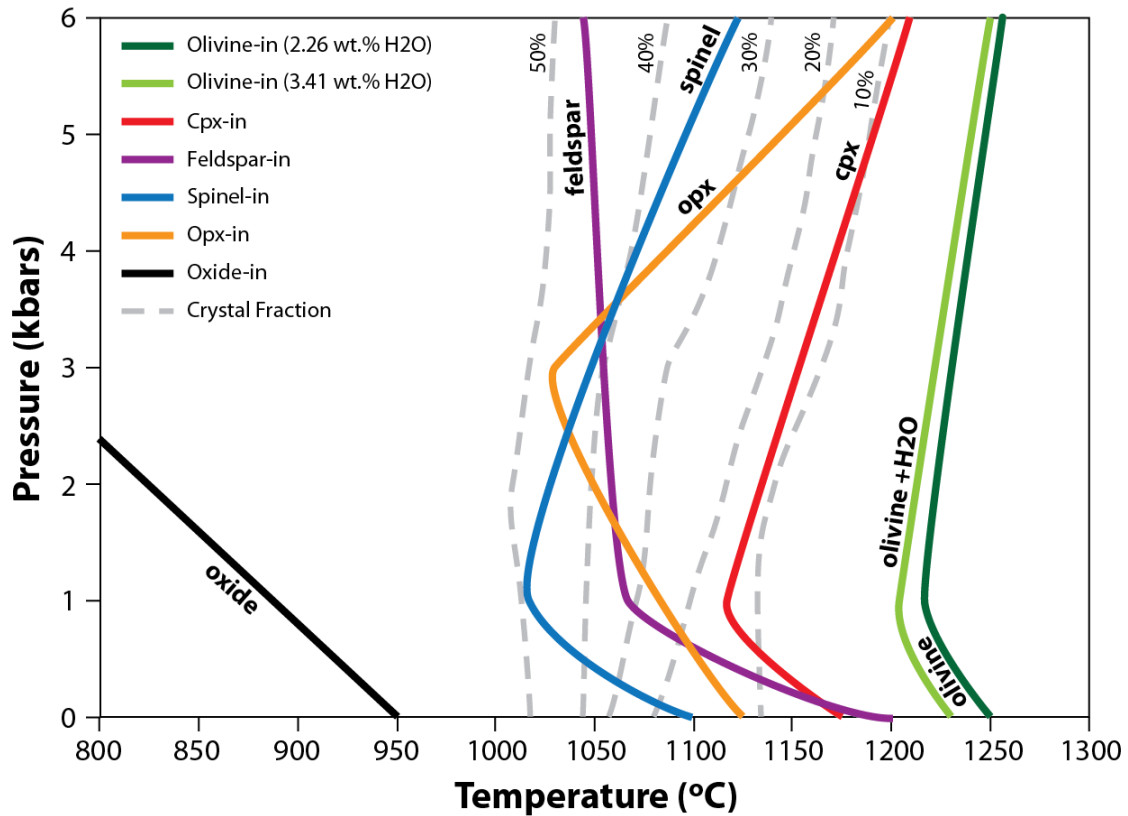


Figure 22. Phase diagram created using the program MELTS and the most primitive (i.e. highest MgO content) melt inclusion data point from K. Walowski (pers. comm.). This phase diagram shows that at low pressures and decreasing temperatures, opx becomes a more stable than plagioclase. This can explain the abundance of small mafic crystals seen in transitional Cinder Cone samples, which imply nucleation without growth. If they formed close to the surface and then were erupted, there would be little time for growth.

diagram shows that, at low pressures and temperatures ($\leq \sim 1$ kbar and $\leq \sim 1100^\circ\text{C}$), orthopyroxene (opx) becomes more stable than plagioclase. This can explain why, especially in the samples around the transition (LCC-1-6 through LCC-1-3), there are abundant, small mafic crystals (Fig. 15); these mafics, which are mostly pyroxenes, crystallized shallowly (≤ 1 kbar of pressure and $\leq 1100^\circ\text{C}$) beneath the volcano and then were erupted without time to grow. In contrast, the plagioclase nucleated deeper (~ 1 -3 kbar and ~ 1050 - 1100°C) and thus had time to grow while being transported to the surface. Therefore, the pre-eruptive transport and storage conditions varied with decreasing depth under the surface of the volcano and, before, during, and after the transition from Unit 2 to Unit 3, included shallow (< 1 kbar), brief ($<$ months) storage that prompted the nucleation of mafic crystals.

Table 3. Composition used in MELTS modeling to create phase diagram (Fig. 22) comes from olivine-hosted melt inclusion.

Oxide	Normalized Wt.%
SiO ₂	49.97
Al ₂ O ₃	16.08
Fe ₂ O ₃	1.35
FeO	5.55
MgO	10.15
CaO	10.49
Na ₂ O	2.60
K ₂ O	0.61
TiO ₂	0.77
MnO	0.07
P ₂ O ₅	0.12

When crystallinity and number density are compared with other characteristics of the deposit (MdΦ and % golden tephra), very few trends emerge (Fig. 23). As previously shown, MdΦ and % golden data can be used to infer eruption style: as MdΦ increases (average clast size decreases) and % golden decreases, explosivity increases (Figs. 18,

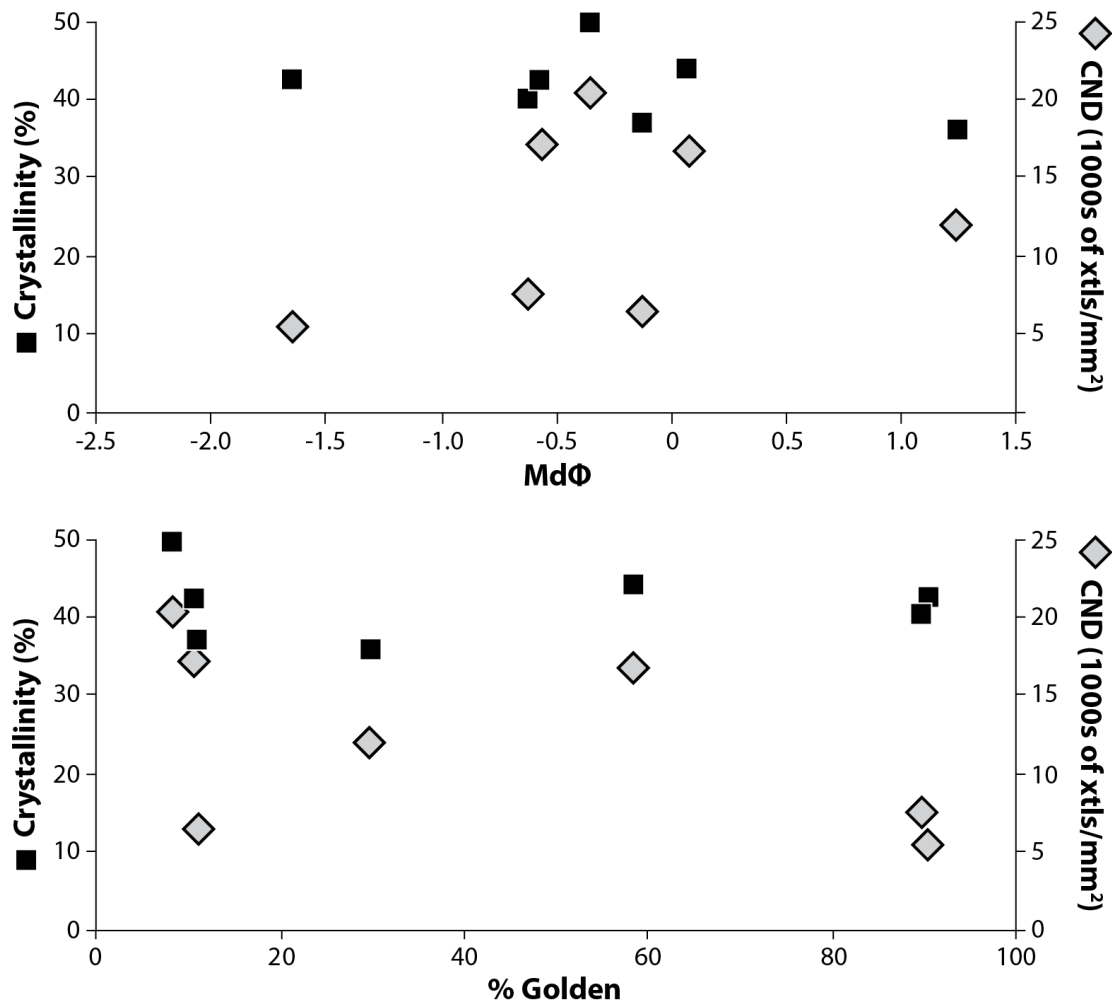


Figure 23. Crystallinity and crystal number density (CND) plotted against MdΦ (top) and % golden tephra (bottom). MdΦ and % golden both correlate with change in eruption style; as MdΦ increases (i.e. average grain size decreases) and % golden increases, explosivity decreases. Though crystallinity remains relatively constant in both plots, meaning that crystallinity is not controlled by eruption style, CND shows a slight trend in that samples with low CND are also those with large grain sizes and high proportions of golden tephra and vice versa meaning that the more explosive the eruption, the higher the CND.

19). Crystallinity remains relatively constant throughout the range of $Md\Phi$ and % golden tephra, indicating that the percentage by area of crystals is not dictated by eruption style (e.g. Hawaiian vs. violent Strombolian). In this limited dataset, CND may show some variation: the largest and most dominantly golden samples also show the lowest CND s while the samples with smaller grain sizes, though not the smallest, and smaller proportions of golden tephra have higher CND s. In this study, changes in CND are controlled primarily by small mafic crystals (Fig. 15), which are mostly pyroxenes.

4.3. Eruption Chronology – the Perspective Provided by Geochemistry

Previous bulk geochemical work has been used to classify different phases of the Cinder Cone eruption (Fig. 3). There are five flows – Old Bench, Painted Dunes 1 and 2, and Fantastic Lava 1 and 2 – and their bulk compositions change from basalt to basaltic andesite and then back to basalt. The compositions of tephra from the three units also follow the lava flow composition trends. Based on observations and data in this study, I will reinterpret the details of Cinder Cone’s eruption progression.

The earliest phase of the eruption captured in this study is represented by tephra sample LCC-1-9, inferred to be the opening phase of Unit 2. The emplacement of the Old Bench (OB) and Painted Dunes 1 (PD1) lava flows occurred during the eruption of Unit 2, probably between samples LCC-1-8L and LCC-1-8U or between LCC-1-8U and LCC-1-7 in this study. LCC-1-8 and LCC-1-7 are both thicker layers of larger golden clasts and thick layers of large golden clasts were deposited directly on top of both OB and PD1 lava flows (Figs. 10b, 17). Of the lavas and tephra, OB is the most primitive in bulk composition (blue squares in Fig. 3), though it does grade directly into PD1 and Unit 2

bulk compositions. The Painted Dunes 1 flow, which is compositionally associated with Unit 2 tephra (Fig. 3), is the second effusive phase of the eruption. As stated, only the OB and PD1 flows are covered in a substantial amount of both Unit 2 and Unit 3 tephra (Fig. 10), though the Unit 2 layers on the flows are oxidized orange and purple and the earliest tephra seems to be welded to the flow. This clast oxidation and welding mean that the eruption of the later part of Unit 2 occurred during or shortly after the effusion of OB and PD1.

Of the lava flows, PD2 temporally follows PD1, however, the compositional trend of PD2 seems to follow the compositional trend of the Fantastic Lava flows better than it does the earlier OB and PD1 flows (Fig. 3). This distinction is supported by the fact that PD2 is not visibly covered in substantial tephra, unlike PD1 and similar to FL1 and FL2 (Fig. 10a). This may mean that most of the Unit 3 tephra erupted prior to the effusion of the PD2, FL1, and FL2 flows. An alternative explanation is that the PD2, FL1, and FL2 flows erupted and cooled before the emission of tephra Unit 3; this seems unlikely, however, given the pattern of intense tephra emission at the beginning of the Parícutin eruption with little tephra emission for the last several years (Pioli et al., 2008) as well as the segregation of the explosive and effusive components of the eruption into two separate vents. It makes sense that, if the volatiles are segregating from the magma, they would rise through the magma and erupt explosively at the vent before leaving the rest of the magma to quietly effuse out of the base of the cone (e.g., Krauskopf, 1948; Pioli et al., 2009). However, Unit 3 tephra compositions mimic the changes in FL lava compositions, which signifies synchronous eruption of both the tephra and the lava. This

discrepancy has yet to be resolved, though may mean that the fine tephra of Unit 3 does exist on later flows, but has fallen into the creviced surfaces of the flows.

Although the details of the Unit 3 and PD2, FL1, and FL1 eruptions have yet to be resolved, it is still clear that the OB and PD1 flows comprise one trend and that the PD2, FL1, and FL2 flows comprise a different trend, instead of OB, PD1 and 2, and FL1 and 2 (Fig. 24). One further issue with the interpretation that OB and PD1 are associated with each other is that there are some tephra Unit 2 samples that have bulk compositions that are similar to PD2. This may mean that the boundary between Units 2 and 3 needs to be revised in the section from which these samples were collected.

In addition to bulk rock geochemical data collected by M. Clynne of the USGS (Fig. 3), a collaborator, K. Walowski, of the University of Oregon has used samples described here in a study on olivine-hosted melt inclusions from Cascade cinder cones. I will present her applicable data, with her permission. Melt inclusions provide information about the composition of the melt prior to eruption and potentially prior to subsurface magmatic processes such as fractionation and contamination. Her data will provide information on magma source and crystallization depths and what the melt compositions were when the host crystals were formed. This information will help to answer questions about the differences between Units 2 and 3, where the crystals formed, and the probably contamination and assimilation of granitic material.

Melt inclusion data show three different populations of host olivine phenocrysts – Fo₈₉₋₉₀ found in Unit 2, Fo₈₂₋₈₄ found in the middle of the eruption, and Fo₈₈₋₈₉ found in Unit 3 – as well as Fo₇₅₋₈₀ rims on all analyzed crystals. As shown in Figure 25 on a diagram of TiO₂ versus SiO₂, melt inclusions are generally much more primitive than

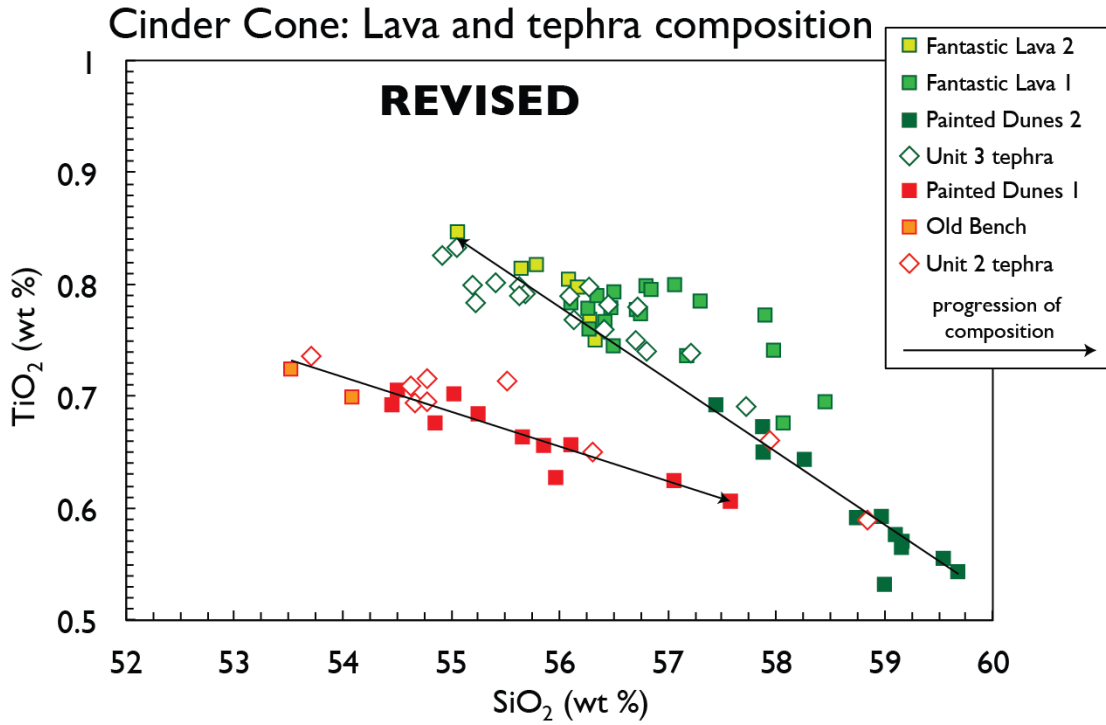


Figure 24. Revised trends in the bulk geochemistry of lava and tephra samples collected by M. Clynne (pers. comm.). Here, I group OB and PD1 flows as one phase of the eruption and PD2, FL1, and FL2 as a different phase.

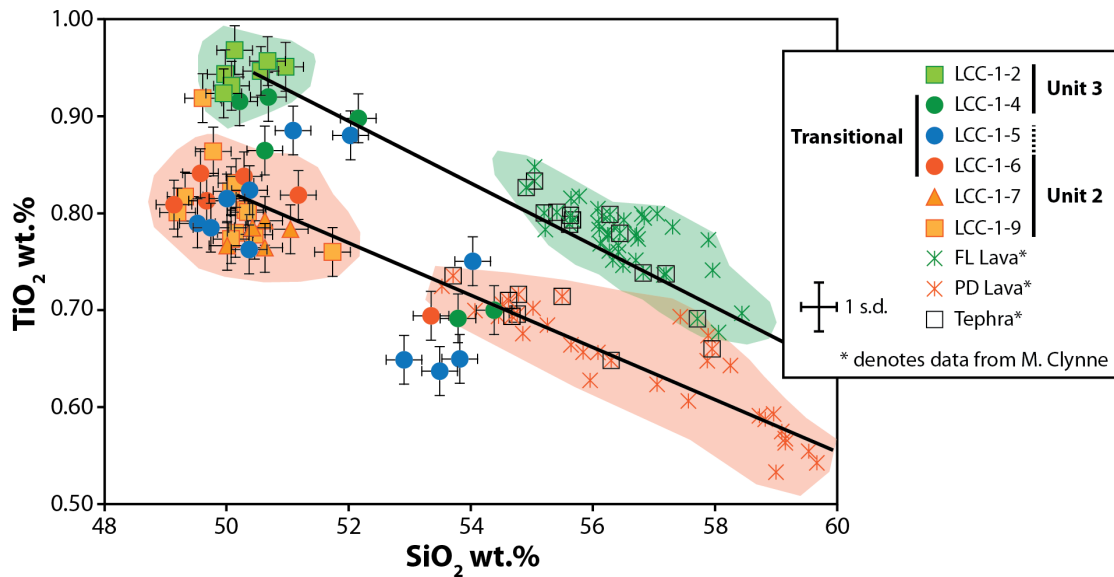


Figure 25. Plot showing bulk composition data from M. Clyne, USGS (orange and green stars and boxes) as well as melt inclusion data from K. Walowski, University of Oregon. (filled shapes). Like the bulk tephra and lava, the melt inclusion compositions separate into two distinct batches, based on TiO_2 , though their more primitive SiO_2 composition is similar. There is a group of contaminated inclusions whose composition is similar to that of early Painted Dunes lava and tephra; these samples span the Unit 2-Unit 3 transition. The black lines are mixing lines drawn from an average melt inclusion composition to the composition of granitic basement that outcrops in the area. These show that much of the change in Cinder Cone lava composition can be attributed to contamination by and assimilation of a granitic country rock. Figure courtesy of K. Walowski.

bulk tephra and lava compositions. TiO_2 is incompatible in crystalline phases in the mantle and should decrease throughout the eruption if Unit 2 and Unit 3 magma were coming from the same mantle source. Instead, melt inclusion compositions segregate into two distinct batches – an earlier batch with lower TiO_2 and a later batch with higher TiO_2 (Fig. 25); two different olivine populations for Units 2 and 3 support this. There are, however, some inclusions in samples LCC-1-5 and LCC-1-4 that are contaminated with additional SiO_2 ; these samples also show lower and varied forsterite compositions. Most of this contamination comes from a granite from the Sierra Nevada basement inferred to underlie much of LAVO (Berge and Stauber, 1987), as shown by the prevalence of xenocrystic quartz and the mixing lines in Figure 25 that connect primitive melt inclusions to the Sierran granite through the Cinder Cone lava flows and tephra compositions.

These contaminated samples span the Unit 2-Unit 3 transition and their evolved compositions indicate increased residence time of the magma at shallower depths beneath the volcanic edifice. Indeed, volatile data show that a few inclusions from samples LCC-1-5 and LCC-1-4 crystallized at low pressures while all other inclusions crystallized between 200-350 MPa or ~8-12 km depth (Fig. 26).

These geochemical data support the physical data presented in this study. Units 2 and 3 are distinct in spatial extent, grain size, and componentry (Fig. 8), which is supported by TiO_2 data showing two different magma batches. Sample LCC-1-4 shows increased crystallinity (Fig. 14) and other samples straddling the Unit 2-Unit 3 transition show increases in small mafic crystals (Fig. 15) which are caused by shallow stalling and crystallization of the magma. These inferences are supported by the geochemical data

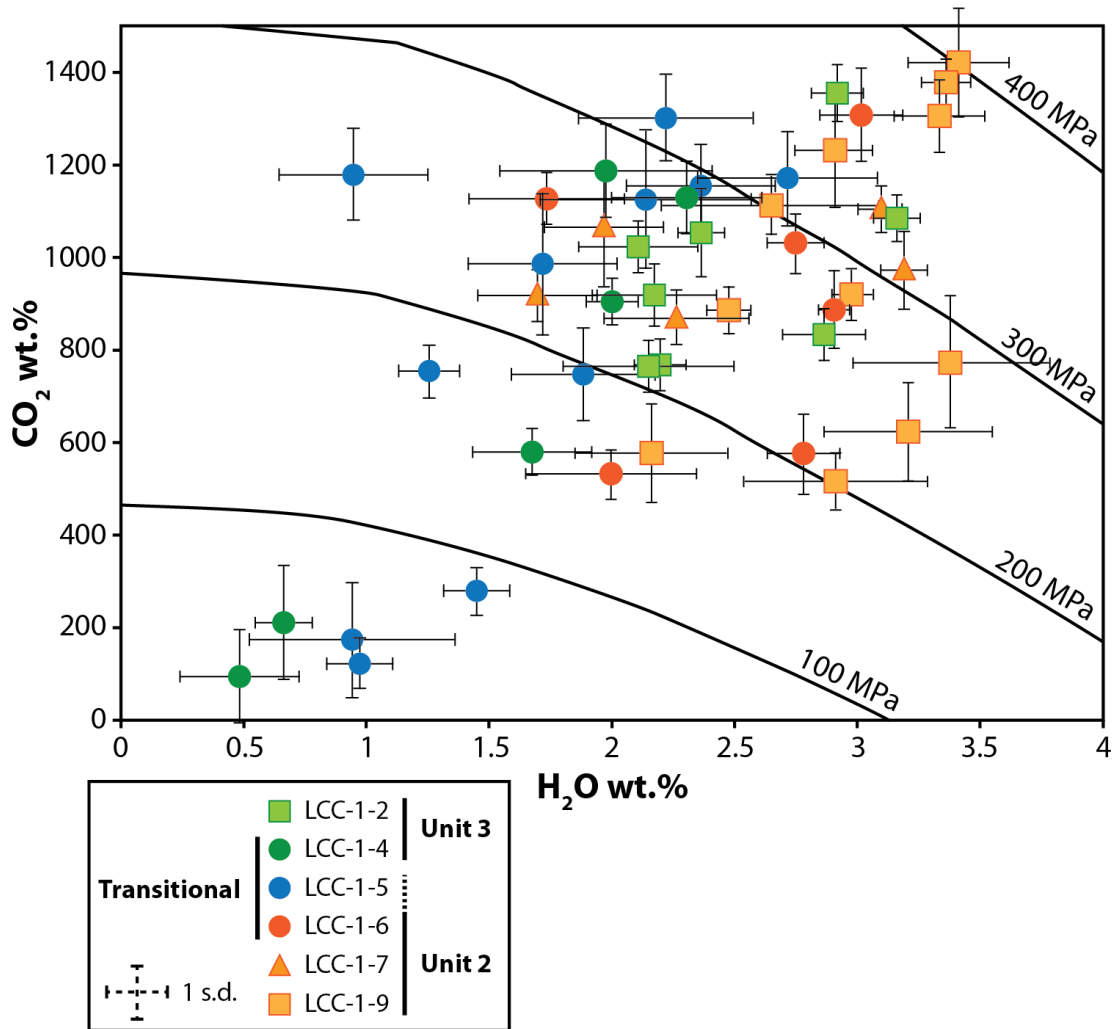


Figure 26. Volatile data shows that most of the melt inclusions analyzed were trapped between 200 and 350 MPa, or ~8-12 km depth. There is a small population of inclusions from samples LCC-1-4 and LCC-1-5 that were trapped at much lower pressures. These correspond to the SiO₂-contaminated inclusions from Figure 21 and show that during the transition from Unit 2 to Unit 3, some magma stalled beneath the edifice and crystallized. Figure courtesy of K. Walowski.

that show a contaminated population of melt inclusions that have lower TiO_2 and higher SiO_2 (Fig. 25), and also crystallized at lower pressures (Fig. 26).

4.4. Eruptive Styles

Mafic eruption styles range from Hawaiian as the least explosive to Plinian as the most explosive. Explosivity and eruption style are determined by the column height, dispersal, grain size of erupted clasts, and even types of clasts erupted. These are influenced by magma composition, volatile abundance, and subsurface processes like magma rise speed, crystallization, contamination and mixing, etc. It is important to determine eruption styles that a specific volcano or volcanoes in an area may produce to be able understand the hazards it/they pose/s to the surrounding community. These data will allow for emergency planning, hazard map creation, and education.

The data and interpretations in this study point to varying eruption style during the creation of Cinder Cone's deposit. Unit 2 was less explosive than Unit 3, as illustrated by the limited spatial extent of the deposit (Fig. 17), the relatively large grain sizes (Figs. 8, 18), and dominance of golden tephra in the Unit 2 samples (Figs. 8, 19). In Figure 17, Unit 2 has a strongly negative slope similar to that of Hawaiian and Strombolian eruptions. Many of the Unit 2 samples plot in the Strombolian field of Figure 18 because of their relatively larger grain sizes. When compared with the componentry of other eruptions, many Unit 2 samples plot with data from Hawaiian eruptions (Fig. 19). Based on these data, the eruption of Unit 2 occurred in a less explosive Hawaiian or Strombolian manner that deposited larger clasts of predominantly golden tephra closer to the vent.

The eruption of Unit 3 was much more voluminous and widespread (Figs. 5, 16), generally finer grained (Figs. 8, 18), and dominated by darker and denser tephra samples (Figs. 8, 19). The Unit 3 deposit has a much wider spatial extent (Fig. 5) and a gentler slope in Figure 16, similar to that of violent Strombolian and subplinian eruptions (Collier Cone and Fuego, 14 October 1974, respectively). All Unit 3 samples plot in the violent Strombolian field when grain size data are compared (Fig. 18) and overlap with Parícutin and Lava Butte data, which have been classified as violent Strombolian eruptions (Pioli et al., 2008; D. McKay, 2012). Comparing components shows that Unit 3 samples are dominated by black and dense tephra, similar to Parícutin data (Fig. 19). Because these components (black and dense tephra, in this study) only seem to appear in the deposits of more explosive (e.g. violent Strombolian) eruptions, it is possible that they are characteristic of increasing explosivity in mafic eruptions (Fig. 19, Pioli et al., 2008). Therefore, Unit 3 erupted in a more explosive violent Strombolian manner, depositing finer grained darker tephra farther away from the vent. Furthermore, it is interesting to note that Cinder Cone and other violent Strombolian cones do show patterns similar to those basaltic eruptions labeled subplinian and Plinian (Fig. 1), though cinder cone deposits collect over periods of weeks to months, and even years.

4.4.1. Formation of different components

All volcanic eruptions produce clasts of different morphologies and characteristics. At Cinder Cone, three main clast components have been identified and compared with other cinder cone components produced by different eruption styles. How these components were created is a question that does not yet have a firm answer, though

the process probably varies across volcanoes. In this section, I will compare data and hypotheses from other workers to observations made at Cinder Cone.

Kilauea Iki, Hawai'i is an example of a Hawaiian-style eruption, and Episode 1 of the eruption displayed lava fountains between 200-300m high for 5 days after initial fissure opening and coalescence into one fountain (Stovall et al., 2011). The components of this eruption are highly vesicular and comparable to the golden tephra of Cinder Cone. Though there is variation between the clasts, the deposits of Kilauea Iki lack the darker and denser tephra of Cinder Cone (Unit 3) and other violent Strombolian eruptions. Stovall et al. (2011) attribute differing clast morphologies to residence time in the fountain: the more vesicular the clast, the longer the clast spent in the fountain, presumably in the center, and the more time the bubbles had to grow. This process perhaps influences component distribution at Cinder Cone during Hawaiian pulses of the eruption, though additional vesicularity data is needed to test this hypothesis.

Explosive deposits from the 2001 eruption of Etna on the island of Sicily in Italy were erupted when a 100-m-high cone was formed by variable eruption style at an elevation of 2550 m a.s.l. The erupted deposits show three distinct phases: the earliest phase is dominated by oxidized, lithic clasts and blocky ash with some hydration cracks and ash aggregates, the middle phase is composed of vesicular, glassy scoria and ash, and the final phase comprises microlite-rich, dense juvenile pyroclasts of low to no vesicularity. Glassy, vesicular scoria (sideromelane; glass = 76.1 vol%) and dense, crystalline pyroclasts (tachylite; glass = 12.6 vol%) are the two end members on a scale of increasing crystallinity that defined eruption style during this eruption at Etna. These components are similar to the golden and dense tephra observed at Cinder Cone (Heiken,

1978), although Cinder Cone also has an additional component, black tephra, which lies between sideromelane and tachylite on vesicularity and crystallinity scales. Based on crystal size distributions, Taddeucci et al. (2004) infer that tachylite is formed by further crystallization of sideromelane, which was quenched prior to additional crystallization. They hypothesize that vesicularity and crystallinity differences occur due to different residence times in the conduit, which is controlled by local magma rise speed and velocity gradients within the conduit. Magma rising relatively faster (e.g. in the center of the conduit) would reach the fragmentation zone near the upper conduit with few microlites and then would rapidly quench and preserve the few small microlites and expanding bubbles. Slower magma rise speeds (e.g. found along the borders of the conduit) allow for increased microlite nucleation and growth, as well as bubble escape and/or collapse. To test whether this process occurs at Cinder Cone, crystal number density data, including crystal size distributions, of the different components are necessary.

In addition to residence time in a fountain and in the conduit, workers have hypothesized other processes to create different tephra components. One of these is the fallback and recycling of pyroclasts in other volcanic vents. At Kilauea Iki, the tephra emission was accompanied by an accumulating lava lake that cycled between filling and draining; tephra that was not deposited fell back into the vent and was potentially re-erupted (Stovall et al., 2011). The creation of the ash fraction of the deposits of El Jorullo volcano in Mexico was due to the recycling and breaking of larger clasts within the vent (Rowland et al., 2009). Clast recycling has also been documented at submarine volcano NW Rota-1; thin sections show microcrystalline inclusions incorporated into microlite-

poor glass (Deardorff et al., 2011). Evidence for clast mingling and recycling at Cinder Cone is shown by inclusions of highly crystalline material in less crystalline material (as described by Deardorff et al., 2011; Fig. 27); examples of mingling are rare in hand specimen, but have been found. Additionally, welded layers that dip into the vent are visible in the crater of Cinder Cone. That these layers are welded indicates that still-liquid lava was falling onto the vent rim, and that the layers are dipping into the vent indicates that some of this lava would have fallen back into the vent. This means that clast recycling is probably an important factor in determining clast morphology and componentry at Cinder Cone.

Finally, a gas segregation mechanism has been proposed for Parícutin (Krauskopf, 1948). This mechanism calls for a shallow dike and sill complex within or directly beneath the volcanic edifice where a majority of the volatiles segregate from the rest of the magma and explode out of a central vent while the degassed magma flows out the base of the edifice. This shallow segregation explains the coeval eruption of both pyroclastic and effusive material, as well as other observations at Parícutin (and other cinder cones). The inferred shallow network of dikes and sills may also be responsible for the different components of the eruption. The black and dense material shows increased crystallinity (Fig. 13), indicating increased residence time. This increased residence time may be caused by magma depositing in the dikes and sills and not erupting until it gets re-entrained in currently erupting magma and carried out of the vent (Pioli et al., 2008). In this manner, different clast components can be erupted at the same time and their changing proportions can provide information about changes in the magma delivery system.

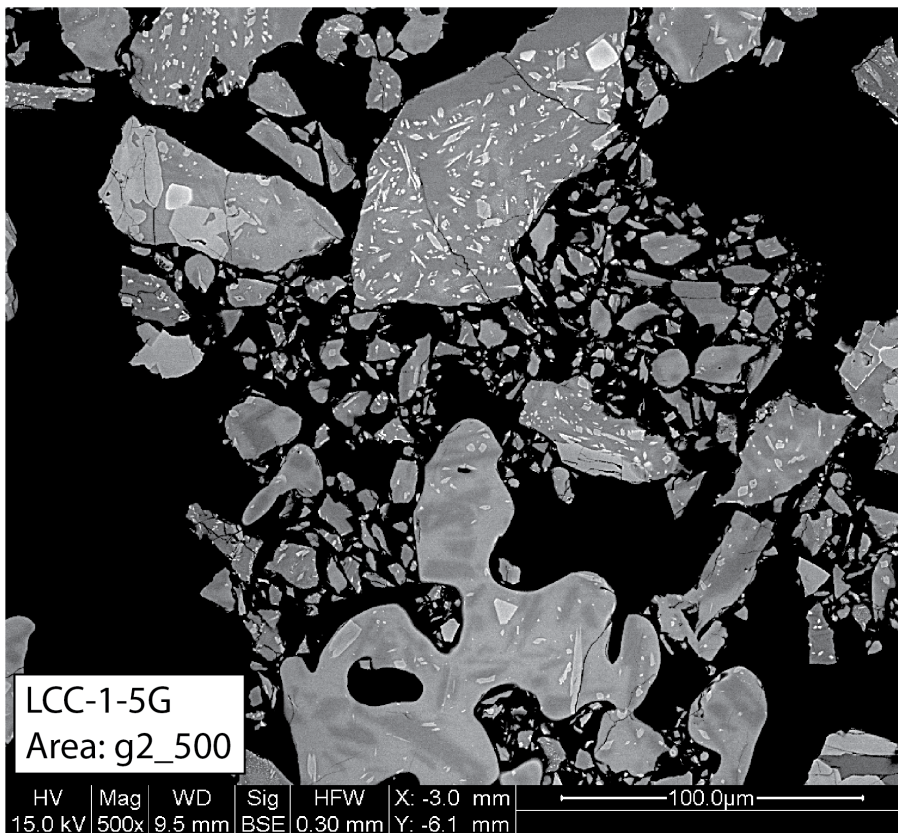
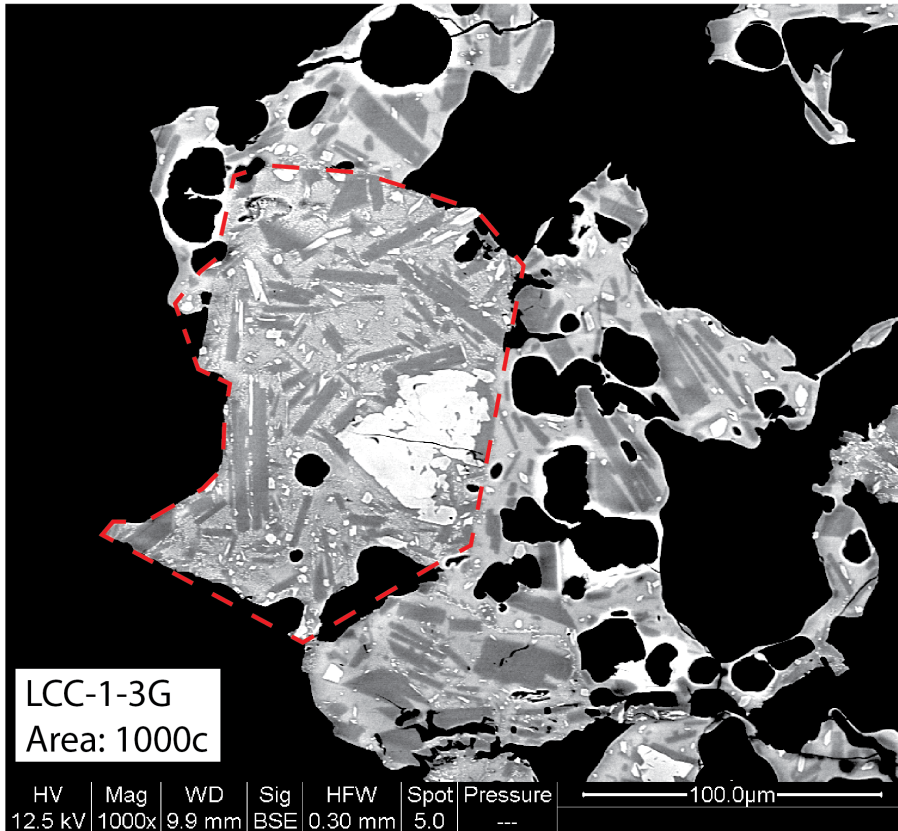


Figure 27. SEM images showing the inclusion of more crystalline material in less crystalline material in Cinder Cone samples (as labeled).

A combination of these proposed processes and others probably occurred to create the components and features of Cinder Cone tephra. Qualitatively, black and dense tephra show increased crystallinity, both of microlites and phenocrysts, and decreased vesicularity (Fig. 13), which can be explained by conduit residence time and shallow gas segregation, among others. Determining the dominant process/es will require further detailed analysis of the different components. Additional crystallinity and vesicularity and number density data will give information regarding ascent and residence time and location beneath the edifice. Crystal and vesicles shapes and sizes will also provide insights into ascent, storage, degassing, and eruption processes. Resolving the processes involved in the formation of tephra and its components will aid in the understanding of (shallow) magma plumbing systems and eruptive processes at cinder cones and other volcanoes, which will inform hazard and risk management.

As intimated, many factors, known and unknown, influence eruptive style. These include volatile content and degassing, conduit size and shape, configuration of the shallow plumbing system, composition of the magma, crystal size, shape, and content, and others. The use of a variety of data types to infer eruption style leads to a more accurate hypothesis. In this study, I used spatial extent, grain size, componentry, and crystal data to infer that the explosive component of Cinder Cone erupted through at least two phases (Unit 2 and Unit 2) and by at least two different eruption styles (Strombolian and violent Strombolian). These inferences will be further informed by understanding the differences between the observed tephra components and their formation.

CHAPTER V

CONCLUSIONS

This study examined the physical characteristics (spatial extent, grain size, componentry, crystal textures) of ten samples collected from the tephra deposit of Cinder Cone, LAVO, and found that the Cinder Cone tephra erupted by varied styles. Unit 2 was less explosive than Unit 3, showing a shift from Hawaiian/Strombolian styles to Strombolian/violent Strombolian styles. Additionally, the geochemistry of olivine-hosted melt inclusions shows that Unit 2 and Unit 3 tephra erupted from different magma batches (Fig. 25). However, all of the erupted material was contaminated by granite from the Sierran basement as shown by abundant quartz xenocrysts. Finally, I have reinterpreted the eruption stratigraphy to place the Old Bench and Painted Dunes 1 flows along the same trend and to add the Painted Dunes 2 flow to the beginning of the Fantastic Lava sequence (Fig. 24). The detailed temporal relationship remains unclear due to discrepancies in geochemical observations between the tephra and the lava.

The eruption of Cinder Cone in northeast LAVO proceeded by at least two, and probably three, different eruption styles. This presents varied hazards to the people and infrastructure of the area, should another cinder cone eruption occur. Because the area is surrounded by a national park and national forests, many outdoor enthusiasts may be in danger and out of contact. The area is covered in trees, so forest fires will be a dangerous hazard. If the eruption is violent enough, fine ash will be produced which will impact air traffic as well as animal and human health. Understanding the details of what may occur and planning efficiently for them may mitigate these hazards. This study seeks

understand the mechanisms behind Cinder Cone's creation and eruption, thereby adding to the hazard data of the area.

Questions concerning this eruption remain partially unresolved. The contamination story is still incomplete and I plan to estimate the amount of granitic material needed to cause the observed compositional changes in Cinder Cone's erupted material. Additionally, I plan to measure the reaction rims of the quartz xenocrysts in thin sections to get an idea of relative changes in contamination. The temporal relationship between the tephra and lava has yet to be fully resolved. I have supplied one interpretation here, but additional fieldwork is necessary to attempt to complete the story. I plan to dig additional pits on the islands in the PD2 and FL1 flows to better constrain the tephra-lava relations.

REFERENCES CITED

- Andronico, D., Cristaldi, A., 2009. Explosive volcanic eruptions: examples of the recent activity at Mt. Etna volcano. Support to Aviation for Ash Avoidance (SAVAA) Meeting.
- Asimow, P.D., Ghiorso, M.S., 1998. Algorithmic modifications extending MELTS to calculate subsolidus phase relations. *American Mineralogist*, 83: 1127-1131.
- Berge, P.A., Stauber, D.A., 1987. Seismic refraction study of upper crustal structure in the Lassen Peak area, northern California. *Journal of Geophysical Research*, 92: 10571-10579.
- Booth, B., Walker, G.P.L., 1973. Ash deposits from the new explosion crater, Etna 1971. *Philosophical Transactions of the Royal Society of London A*, 247: 147-151.
- Brenna, M., Cronin, S.J., Smith, I.E.M., Sohn, Y.K., Németh, K., 2010. Mechanisms driving polymagmatic activity at a monogenetic volcano, Udo, Jeju Island, South Korea. *Contributions to Mineralogy and Petrology*, 160: 931-950.
- Calvari, S., Pinkerton, H., 2004. Birth, growth and morphologic evolution of the 'Laghetto' cinder cone during the 2001 Etna eruption. *Journal of Volcanology and Geothermal Research*, 132: 225-239.
- Clynne, M. A., Champion, D.E., Trimble, D.A., Hendley, J.W. II, Stauffer, P.H., 2000. How Old is "Cinder Cone"?—Solving a Mystery in Lassen Volcanic National Park, California. U.S. Geological Survey Fact Sheet 023-00, 4 p.
- Clynne, M.A., Christiansen, R.L., Trimble, D.A., and McGeehin, J.P., 2002. Radiocarbon dates from volcanic deposits of the Chaos Crags and Cinder Cone eruptive sequences and other deposits, Lassen Volcanic National Park and vicinity, California. U.S. Geological Survey Open-file Report 02-290, 18 p.
- Clynne, M.A., Muffler, L.J.P., 2010. Geologic Map of Lassen Volcanic National Park and Vicinity, California. Scientific Investigations Map 2899.
- Clynne, M.A., Bleick, H., 2011. Stratigraphy and compositional evolution of Cinder Cone, a composite monogenetic cone in Lassen Volcanic National Park, California. AGU Fall Meeting.
- Costantini, L., Bonadonna, C., Houghton, B.F., Wehrmann, H., 2009. New physical characterization of the Fontana Lapilli basaltic Plinian eruption, Nicaragua. *Bulletin of Volcanology*, 71: 337-355.

- D’Oriano, C., Bertagnini, A., Pompilio, M., 2011. Ash erupted during normal activity at Stromboli (Aeolian Islands, Italy) raises questions on how the feeding system works. *Bulletin of Volcanology*, 73: 471-477.
- Deardorff, N.D., Cashman, K.V., Chadwick Jr., W.W., 2011. Observations of eruptive plume dynamics and pyroclastic deposits from submarine explosive eruptions at NW Rota-1, Mariana arc. *Journal of Volcanology and Geothermal Research*, 202: 47-59.
- Diller, J.S., 1891. A Late Volcanic Eruption in Northern California and its Peculiar Lava. *U.S. Geological Survey Bulletin* 79, 33p.
- Edbrooke, S.W., Mazengarb, C., Stephenson, W., 2003. Geology and geological hazards of the Auckland urban area, New Zealand. *Quaternary International*, 103: 3-21.
- Finch, R.H., Anderson, C.A., 1930. The Quartz Basalt Eruption of Cinder Cone, Lassen Volcanic National Park, California. *University of California Publications in Geologic Sciences*, 19: 245-273.
- Forshag, W.F., González R., J., 1956. Birth and Development of Parícutin Volcano Mexico. *U.S. Geological Survey Bulletin* 965-D.
- Ghiorso, M.S., Sack, R.O., 1995. Chemical mass transfer in magmatic processes. IV. A revised and internally consistent thermodynamic model for the interpolation and extrapolation of liquid-solid equilibria in magmatic systems at elevated temperatures and pressures. *Contributions to Mineralogy and Petrology*, 119: 197-212.
- Hammer, J.E., Cashman, K.V., Hoblitt, R.P., Newman, S., 1999. Degassing and microlite crystallization during pre-climactic events of the 1991 eruption of Mt. Pinatubo, Philippines. *Bulletin of Volcanology*, 60: 355-380.
- Hasenaka, T., Carmichael, I.S.E., 1985. The cinder cones of Michoacán-Guanajuato, central Mexico: their age, volume and distribution, and magma discharge rate. *Journal of Volcanology and Geothermal Research*, 25: 105-124.
- Hill, B.E., Connor, C.B., Jarzempa, M.S., La Femina, P.C., Navarro, M., Strauch, W., 1998. 1995 eruptions of Cerro Negro volcano, Nicaragua, and risk assessment for future eruptions. *Geological Society of America Bulletin*, 110: 1231–1241.
- Houghton, B.F., Wilson, C.J.N., Pyle, D.M., 2000. Pyroclastic Fall Deposits *in* *Encyclopedia of Volcanoes*, Sigurdsson, H., ed. Academic Press: San Diego, CA. 1417 pp.

- Houghton, B.F., Wilson, C.J.N., Del Carlo, P., Coltelli, M., Sable, J.E., Carey, R., 2004. The influence of conduit processes on changes in style of basaltic Plinian eruptions: Tarawera 1886 and Etna 122 BC. *Journal of Volcanology and Geothermal Research*, 137: 1-14.
- Houghton, B.F., Bonadonna, C., Gregg, C.E., Johnston, D.M., Cousins, W.J., Cole, J.W., Del Carlo, P., 2006. Proximal tephra hazards: Recent eruption studies applied to volcanic risk in the Auckland volcanic field, New Zealand. *Journal of Volcanology and Geothermal Research*, 155: 138-149.
- Houghton, B.F., Gonnerman, H.M., 2008. Basaltic explosive volcanism: Constraints from deposits and models. *Chemie der Erde - Geochemistry*, 68: 117-140.
- James, D.E., 1966. Geology and Rock Magnetism of Cinder Cone Lava Flows, Lassen Volcanic National Park, California. *Geological Society of America Bulletin*, 77: 303-312.
- Johnson, E.R., Wallace, P.J., Cashman, K.V., Delgado Granados, H., 2010. Degassing of volatiles (H₂O, CO₂, S, Cl) during ascent, crystallization, and eruption at mafic monogenetic volcanoes in central Mexico. *Journal of Volcanology and Geothermal Research*, 197: 225-238.
- Kervyn, M., Ernst, G.G.J., Carracedo, J.-C., Jacobs, P., 2012. Geomorphometric variability of “monogenetic” volcanic cones: Evidence from Mauna Kea, Lanzarote and experimental cones. *Geomorphology* 136: 59-75.
- Krauskopf, K.B., 1948. Mechanism of eruption at Parícutin Volcano, Mexico. *Geological Society of America Bulletin*, 59: 711-732.
- Lockwood, J.P., Hazlett, R.W., 2010. *Volcanoes: Global Perspectives*. Wiley-Blackwell: Chichester, West Sussex, UK. 539 pp.
- Luhr, J.F., Simkin, T., eds., 1993. *Parícutin: The Volcano Born in a Mexican Cornfield*. Geoscience Press, Inc., Phoenix, AZ.
- Macdonald, G.A., 1972. *Volcanoes*. Prentice-Hall Inc.: Englewood Cliffs, NJ. 510 pp.
- Mangan, M.T., Cashman, K.V., 1996. The structure of basaltic scoria and reticulite and inferences for vesiculation, foam formation, and fragmentation in lava fountains. *Journal of Volcanology and Geothermal Research*, 73: 1-18.
- McGetchin, T.R., Settle, M., Chouet, B., 1974. Cinder Cone Growth Modeled after Northeast Crater, Mount Etna, Sicily. *Journal of Geophysical Research*, 79: 3257-3272.

- Mckay, D., 2012. Recent Mafic Eruptions at Newberry Volcano and in the Central Oregon Cascades: Physical Volcanology and Implications for Hazards. Ph.D. Thesis, University of Oregon, Eugene, OR, USA.
- Needham, A.J., Lindsay, J.M., Smith, I.E.M., Augustinus, P., Shane, P.A., 2011. Sequential eruption of alkaline and sub-alkaline magmas from a small monogenetic volcano in the Auckland Volcanic Field, New Zealand. *Journal of Volcanology and Geothermal Research*, 201: 126-142.
- Ort, M.H., Elson, M.D., Anderson, K.C., Duffield, W.A., Hooten, J.A., Champion, D.E., Waring, G., 2008. Effects of scoria cone eruptions on nearby human communities. *Geological Society of America Bulletin*, 120: 476-486.
- Parfitt, E.A., 1998. A study of clast size distribution, ash deposition and fragmentation in a Hawaiian-style volcanic eruption. *Journal of Volcanology and Geothermal Research*, 84: 197-208.
- Pioli, L., Erlund, E., Johnson, E., Cashman, K., Wallace, P., Rosi, M., Delgado Granados, H., 2008. Explosive dynamics of violent Strombolian eruptions: The eruption of Parícutin Volcano 1943–1952 (Mexico). *Earth and Planetary Science Letters*, 271: 359-368.
- Pioli, L., Azzopardi, B.J., Cashman, K.V., 2009. Controls on the explosivity of scoria cone eruptions; magma segregation at conduit junctions. *Journal of Volcanology and Geothermal Research*, 186: 407-415.
- Pyle, D.M., 1989. The thickness, volume, and grainsize of tephra fall deposits. *Bulletin of Volcanology*, 51: 1-15.
- Rasband, W.S., 1997-2011. ImageJ, U. S. National Institutes of Health, Bethesda, MD, <http://imagej.nih.gov/ij/>.
- Rose, W.I., Self, S., Murrow, P.J., Bonadonna, C., Durant, A.J., Ernst, G.G.J., 2008. Nature and significance of small volume fall deposits at composite volcanoes: Insights from the October 14, 1974 Fuego eruption, Guatemala. *Bulletin of Volcanology*, 70: 1043-1067.
- Rowland, S.K., Jurado-Chichay, Z., Ernst, G., Walker, G.P.L., 2009. Pyroclastic deposits and lava flows from the 1759– 1774 eruption of El Jorullo, México: aspects of ‘violent Strombolian’ activity and comparison with Parícutin *in* *Studies in Volcanology: The Legacy of George Walker*. Special Publications of IAVCEI, 2: 105-128.
- Sheppard, P.R., Ort, M.H., Anderson, K.C., Clynne, M.A., May, E.M., 2009. Multiple dendrochronological responses to the eruption of Cinder Cone, Lassen Volcanic National Park, California. *Dendrochronologia*, 27: 213-221.

- Spörli, K.B., Eastwood, V.R., 1997. Elliptical boundary of an intraplate volcanic field, Auckland, New Zealand. *Journal of Volcanology and Geothermal Research*, 79: 169–179.
- Stovall, W.K., Houghton, B.F., Gonnerman, H., Fagents, F.A., Swanson, D.A., 2011. Eruption dynamics of Hawaiian-style fountains: the case study of episode 1 of the Kilauea Iki 1959 eruption. *Bulletin of Volcanology*, 73: 511-529.
- Taddeucci, J., Pompilio, M., Scarlato, P., 2004a. Conduit processes during the July–August 2001 explosive activity of Mt. Etna (Italy): inferences from glass chemistry and crystal size distribution of ash particles. *Journal of Volcanology and Geothermal Research*, 137: 33–54.
- Valentine, G.A., Krier, D., Perry, F.V., Heiken, G., 2005. Scoria cone construction mechanisms, Lathrop Wells volcano, southern Nevada, USA. *Geology*, 33: 629-632.
- Walker, G.P.L., 1973. Explosive volcanic eruptions – a new classification scheme. *Geologische Rundschau*, 62: 431-446.